Issue 1, January 2026

MATERIALS & STRUCTURAL INTEGRITY

RESEARCH PREPRINTS

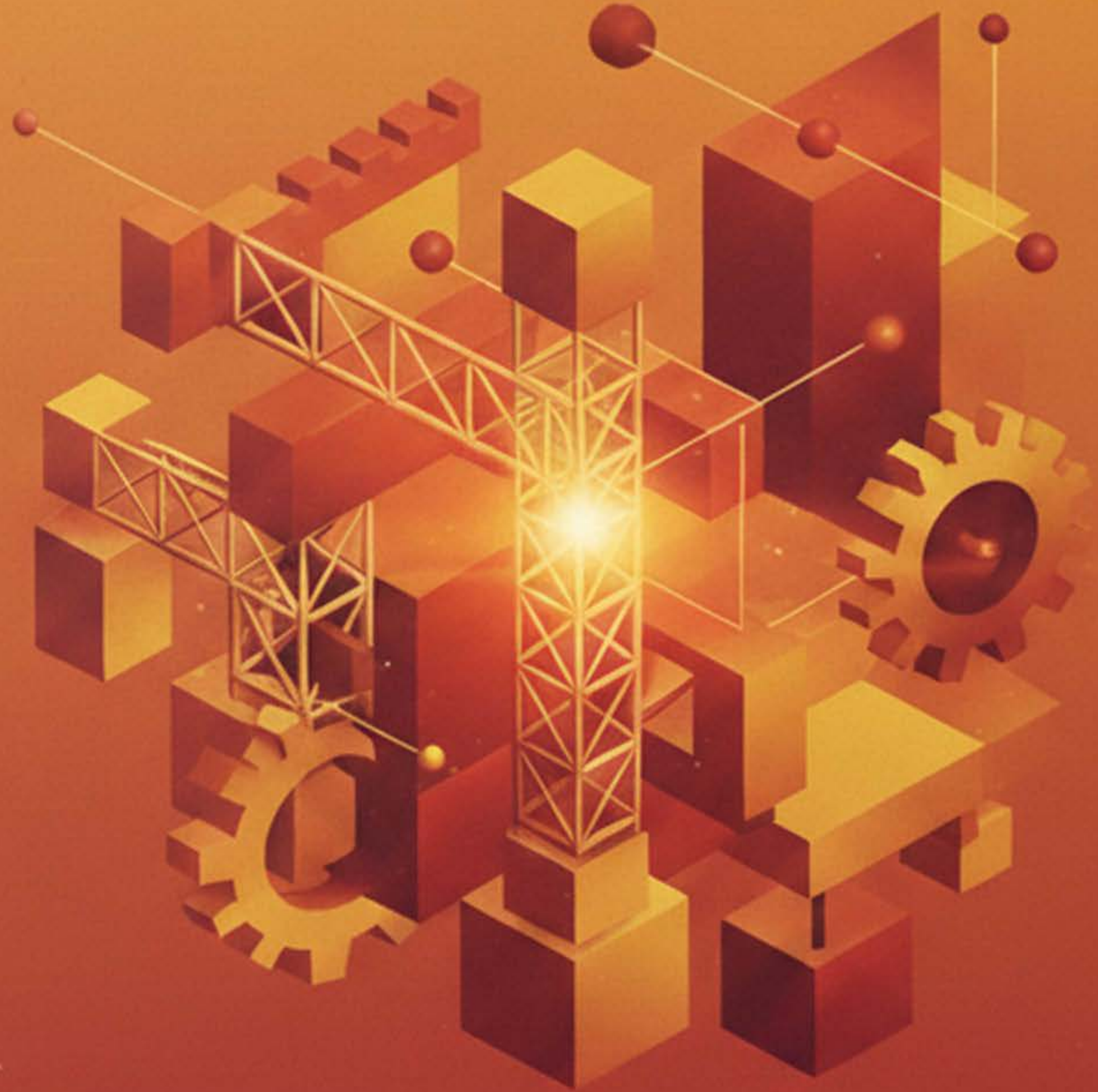

ESIS

JOURNAL DESCRIPTION AND AIMS

Materials and Structural Integrity: Research Preprints is published by the European Structural integrity Society (ESIS) . It is an open-access Journal published on-line four time per year (January, April, July, October).

Materials and Structural Integrity: Research Preprints encompasses the broad topic of structural integrity, which is based on the mechanics of fatigue and fracture and is concerned with the reliability and effectiveness of structural components. The journal publishes collection of preprints submitted to the ESIS platform ESIS-PS (https://www.esis-ps.eu/).

EDITORIAL TEAM

PUBLISHER

European Structural Integrity Society (ESIS)
https://www.esis.site/
via G. Di Biasio 43, 03043, Cassino (FR), Italy

Optimization of functionally graded materials to make stress concentration vanish in a plate with circular hole

Hassan Mohamed Abdelalim Abdalla[1], Francesco De Bona[2], Daniele Casagrande[3]

Polytechnic Department of Engineering and Architecture, University of Udine, Via delle Scienze 206, 33100 Udine, Italy.

Abstract: This paper is devoted to the minimization of the stress concentration factor in infinite plates with circular hole made of functionally graded materials and subjected to a far-field uniform uniaxial tension. Despite the vast literature on the versatility of these materials, the novelty of the results is that the optimal material distribution is not limited to prefixed laws, as in many works available in the literature. It is assumed to be an unknown piecewise constant function, thus aiming to derive the material distribution by exploiting, at best, the inhomogeneity concept associated with functionally graded materials. After a brief review of the governing equations, the motivation, the statement and the mathematical formulation of the optimization problem are given under the hypothesis of axisymmetric material distribution. Still, the problem could not be solved analytically, therefore a direct transcription approach by the aid of finite difference method has been followed to convert it into a nonlinear programming problem, whose solution has been obtained numerically by dedicated gradient-based solvers. Numerical solutions are reported in graphical forms, thoroughly discussed and validated by means of the finite element method. The developed numerical approach yields a material inhomogeneity obeying a sigmoid-like function and a uniform hoop stress along the radial direction, thus making the stress concentration factor at the rim of the circular hole vanish.

Keywords: Functionally graded materials; stress concentration factor; direct transcription; optimization; nonlinear programming; plates.

---

1. Introduction

The study of the stress concentration in panels due to the presence of circular holes constitutes one of the classic problems in mechanics. It is known that if the panel is infinitely large and made of a homogenous, linearly elastic and isotropic material and subjected to a uniform uniaxial tension, then the stress concentration factor (hereinafter

[1] abdalla.hma@spes.uniud.it (ORCID: 0000-0001-7955-955X)
[2] francesco.debona@uniud.it (ORCID: 0000-0002-6829-6122)
[3] daniele.casagrande@uniud.it (ORCID: 0000-0001-6651-1012)

abbreviated by SCF) is identically 3. In literature, this result is commonly referred to as the Kirsch solution, named after the German engineer who first described the elastic stresses around the hole [1]. Since then, engineers and researchers have been interested in reducing such a factor by abandoning the aforementioned isotropic and homogeneity assumptions and the shape of the geometrical discontinuity (see, e.g., [2,3] for an exhaustive literature review on various analytical methods).

The adoption of functionally graded materials has propounded its application to numerous mechanical and geotechnical models [4-6], where the microstructure was allowed to vary along one or several directions by employing isotropic, orthotropic or even anisotropic constituent materials (see, e.g., [7-9]). Among all, the stress analysis of functionally graded panels with holes has been investigated. Several analytical and numerical efforts have been carried out aiming at reducing the stress concentration by taking advantage of different inhomogeneity models. For instance, the effect of the material inhomogeneity on the SCF due to circular and elliptic holes are predicted in [10] and [11], respectively, both by means of the finite element method. In particular, Young's modulus has been allowed to vary spatially. Authors have shown that a reduction in the SCF can be obtained by properly choosing the tuning parameters of the heterogeneity factors associated with the property variations (e.g., the exponents in the power- and exponential laws). In [12], the SCF around a circular hole in an infinite plate subjected to uniform biaxial tension and pure shear is analytically solved by exploiting Frobenius series. Closed-form solutions are derived for an exponential variation of Young's modulus along the radius. By dividing the functionally graded plate into a series of piecewise homogeneous radial layers, Ref. [13,14] report the SCFs due to circular holes and under constant loads by means of Muskhelishvili method of the complex variable functions. In [15], closed-form solutions for the SCF at a circular hole in functionally graded panels subject to a uniform far-field tensile traction are derived by using hypergeometric functions and Frobenius series. Authors show that the SCF at the circular hole can be considerably reduced by appropriately grading the mechanical properties along the radial direction. The elastic response of a functionally graded annular ring inserted in a hole of a homogeneous plate is derived analytically in [16,17] under different far-field loading conditions. All the aforementioned works report a considerable stress concentration reduction only when the Young's modulus progressively increases away from the hole. Moreover, it is observed that the variation of the Poisson's ratio on the stress distribution in the plate is negligible [15-17].

The aforementioned considerations bring into mind the possibility of exploiting optimization theory to enhance the elastic performance of such structures. Many solutions have been proposed to different problems [18,19], some of which are capable of handling only one-dimensional material distribution with one-dimensional geometry and simple loads, while others can tackle more sophisticated problems. Interesting results in terms of stress reduction have been achieved when considering models such as beams, cylindrical shells, rotating disks, pressure vessels and plates (see, e.g., [20-34]), however by imposing prefixed laws for the variation of mechanical properties. In this way, the optimization problems reduce to the search for the heterogeneity factors associated with functional models describing these property variations. On the other hand, other works dealt with the search for the best material distribution to enhance the elastic stress performance *without* prefixing the functional model. Some of these are developed within an analytical tailoring framework [35,36], whereas others rely on phase-field and topology optimization [37,38] or exploit principles from the optimal control theory [39-41]. As far as infinite plates with a circular hole are concerned, the overwhelming research works impose the Young's modulus a priori to forecast the stress concentration near the hole. Only in Ref. [35], an analytical solution is proposed for the cylinder under pressure, whose validity can equivalently hold for the case of biaxially loaded plates. In the uniaxial load case, to the extent of the authors' knowledge, Ref. [42] is the only work where the unknown Young's modulus distribution is sought in plates with different holes and cutouts, in which enhanced stress results have been obtained by developing an evolutionary algorithm combined with the finite element method. It is worth noting that the iteration process for updating the Young's modulus in each element was governed by a power-law function of local and global stress measures. The stiffness was thus reduced only in the elements whose stresses were higher than an imposed threshold. Although this rule-of-thumb stiffness modification led to enhanced SCFs, we strongly believe that optimal solutions can be achieved if the stiffness optimization is carried out in a more global sense. Accordingly, the objective of the present article is to seek the Young's modulus distribution around the circular hole such that the hoop stress reaches its minimum value along prescribed directions.

The article is organized as follows. Section 2 recalls the governing equations for the plane stresses in linearly elastic, isotropic and inhomogeneous plates. Section 3 aims at presenting the motivation of the work as well as the formulation of the optimization problem. Section 4 illustrates the direct transcription approach as a numerical procedure to convert the optimization problem into a nonlinear programming problem, whose solution has been computed by resorting to a solver available in the literature. The optimal solution of a study case, its validation by a finite element model and its discussion are shown in Section 5 and conclusions are drawn in Section 6.

2. Governing equations

Consider a linearly elastic, isotropic and functionally graded infinite plate with a circular hole of radius a. Let the thickness of the plate be sufficiently small to the point that the stress state is two-dimensional (plane-stress condition). Let the plate be subject to a far-field uniaxial traction σ_0, as shown in Figure 1a, where the generic point P is described by the polar coordinate system (r, θ), whose origin is at the center of the circular hole, and MN denotes the vertical line associated with the polar angle $\theta = \pi/2$. Moreover, let the inhomogeneity be described by the radial variation of the volume fraction $V(r)$ of one of the two constituents of the functionally graded material (e.g. material #2), which in turn are linked to the effective Young's modulus $E(r)$ by the well-known rule of mixture

$$E(r) = \tilde{E}_1(1 - V(r)) + \tilde{E}_2 V(r)\,, \tag{1}$$

where $\tilde{E}_1$ and $\tilde{E}_2$ denote the Young's moduli of the constituents (e.g., metallic and ceramic materials), while the Poisson's ratio ν is assumed to be constant and not affected by the volume fraction. It is worthwhile to note Eq. (1) is adopted in this study since it can be considered as the simplest homogenization technique among the several approaches in micromechanics [43].

2.1. Equilibrium, constitutive and compatibility equations

Next, equations describing the mechanical behavior of the plate are listed. In the absence of body forces, the equilibrium equations read [44]

$$\frac{\partial \sigma_r(r,\theta)}{\partial r} + \frac{1}{r}\frac{\partial \sigma_{r\theta}(r,\theta)}{\partial \theta} + \frac{\sigma_r(r,\theta) - \sigma_\theta(r,\theta)}{r} = 0\,, \tag{2a,b}$$

$$\frac{\partial \sigma_{r\theta}(r,\theta)}{\partial r} + \frac{1}{r}\frac{\partial \sigma_{\theta}(r,\theta)}{\partial \theta} + \frac{2}{r}\sigma_{r\theta}(r,\theta) = 0\,,$$

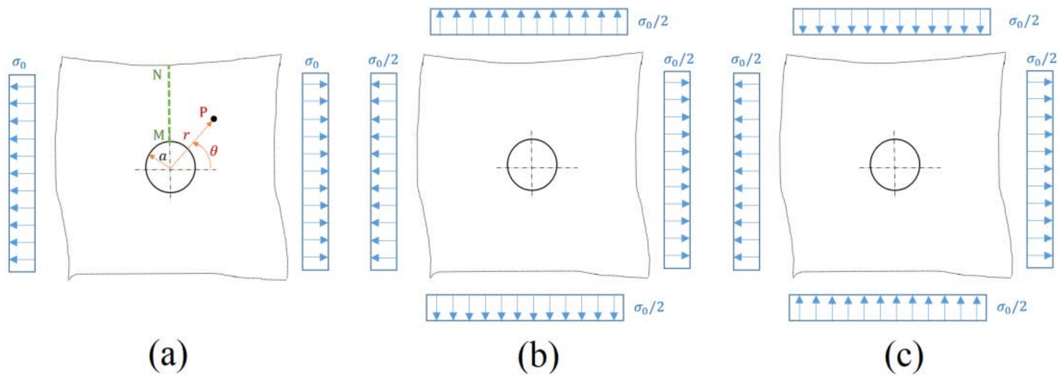

Fig. 1: A schematic representation of (a) an infinite plate with a circular hole subject to a far-field uniaxial traction and its split into (b) uniform biaxial and (c) pure shear sub-problems.

where σ_r, σ_θ and $\sigma_{r\theta}$ are the radial, hoop and shear stresses, respectively, all functions of the radial r and circumferential θ coordinates. The elastic stresses are related to the corresponding strains by the plane-stress constitutive equations, namely [44]

$$\begin{aligned} E(r)\,\varepsilon_r(r,\theta) &= \sigma_r(r,\theta) - \nu\,\sigma_\theta(r,\theta)\,, \\ E(r)\,\varepsilon_\theta(r,\theta) &= \sigma_\theta(r,\theta) - \nu\,\sigma_r(r,\theta)\,, \\ E(r)\,\varepsilon_{r\theta}(r,\theta) &= 2(1+\nu)\,\sigma_{r\theta}(r,\theta)\,, \end{aligned} \tag{3a-c}$$

where ε_r, ε_θ and $\varepsilon_{r\theta}$ are the radial, hoop and shear strains, respectively, which obey the following compatibility equation [44]

$$\frac{\partial^2 \varepsilon_\theta}{\partial r^2} + \frac{1}{r^2}\frac{\partial^2 \varepsilon_r}{\partial \theta^2} + \frac{2}{r}\frac{\partial \varepsilon_\theta}{\partial r} - \frac{1}{r}\frac{\partial \varepsilon_r}{\partial r} = \frac{1}{r}\frac{\partial^2 \varepsilon_{r\theta}}{\partial r \partial \theta} + \frac{1}{r^2}\frac{\partial \varepsilon_{r\theta}}{\partial \theta}\,. \tag{4}$$

2.2. Superposition of stresses

Due to the linearity hypothesis, if the elastic problem is split into two sub-problems, namely the biaxial problem (Figure 1b) and the pure shear problem (Figure 1c), the superposition of their solutions leads to the solution of the original one. In other words, letting superscripts "*bx*" and "*ps*" denote respectively the uniform biaxial and pure shear terms, stresses can be written as

$$\begin{aligned} \sigma_r(r,\theta) &= \sigma_r^{bx}(r) + \sigma_r^{ps}(r,\theta)\,, \\ \sigma_\theta(r,\theta) &= \sigma_\theta^{bx}(r) + \sigma_\theta^{ps}(r,\theta)\,, \\ \sigma_{r\theta}(r,\theta) &= \sigma_{r\theta}^{ps}(r,\theta)\,, \end{aligned} \tag{5a-c}$$

where it is emphasized that stresses for the biaxial problem depend on the radial coordinate only, since the geometry of the problem, the assumed nature of the inhomogeneity and the far-field loading are axisymmetric (and therefore $\sigma_{r\theta}^{bx}$ is identically zero). Substitution of the constitutive relations (3a-c) into the compatibility equation (4) yields the following boundary-value problem for the radial stress

$$\begin{aligned} &\mathcal{BX}(\sigma_r^{bx}(r)) = 0\,, \qquad\qquad a \le r < \infty \\ &\sigma_r^{bx}(a) = 0\,, \\ &\lim_{r\to\infty} \sigma_r^{bx}(r) = \frac{\sigma_0}{2}\,, \end{aligned} \tag{6a-c}$$

where the differential operator $\mathcal{BX}(\cdot)$ is given by $\frac{d^2(\cdot)}{dr^2} + \alpha^{bx}(r)\frac{d(\cdot)}{dr} + \beta^{bx}(r)\,(\cdot)$ with $\alpha^{bx} = \frac{3}{r} - \frac{1}{E}\frac{dE}{dr}$ and $\beta^{bx} = (\nu - 1)\frac{1}{rE}\frac{dE}{dr}$.

Moreover, the hoop stress can be obtained from the equilibrium equation (2a)

$$\sigma_\theta^{bx}(r) = \sigma_r^{bx}(r) + r\frac{d\sigma_r^{bx}(r)}{dr}. \tag{7}$$

In parallel, and similar to the Kirsch solution, the pure shear problem can be solved by introducing the Airy stress function $\varphi(r,\theta)$ as follows [44]

$$\begin{aligned} &\sigma_r^{ps}(r,\theta) = \frac{1}{r}\frac{\partial\varphi(r,\theta)}{\partial r} + \frac{1}{r^2}\frac{\partial^2\varphi(r,\theta)}{\partial\theta^2}\,, \\ &\sigma_\theta^{ps}(r,\theta) = \frac{\partial^2\varphi(r,\theta)}{\partial r^2}\,, \\ &\sigma_{r\theta}^{ps}(r,\theta) = -\frac{\partial}{\partial r}\left(\frac{1}{r}\frac{\partial\varphi(r,\theta)}{\partial\theta}\right), \end{aligned} \tag{8a-c}$$

where φ has the form [44]

$$\varphi(r,\theta) = g(r)\cos 2\theta. \tag{9}$$

Consequently, Eqs. (8a-c) read

$$\begin{aligned} &\sigma_r^{ps}(r,\theta) = \left(\frac{1}{r}\frac{dg(r)}{dr} - \frac{4g(r)}{r^2}\right)\cos 2\theta, \\ &\sigma_\theta^{ps}(r,\theta) = \frac{d^2g(r)}{dr^2}\cos 2\theta, \\ &\sigma_{r\theta}^{ps}(r,\theta) = 2\left(\frac{1}{r}\frac{dg(r)}{dr} - \frac{g(r)}{r^2}\right)\sin 2\theta. \end{aligned} \tag{10a-c}$$

Combining Eqs. (10a-c) and (3a-c), the compatibility equation (4) reduces to the following differential equation

$$\mathcal{PS}(g(r)) = 0\,, \qquad\qquad a \le r < \infty \qquad (11)$$

where the differential operator $\mathcal{PS}(\cdot)$ is given by $\frac{d^4(\cdot)}{dr^4} + \alpha^{ps}(r)\frac{d^3(\cdot)}{dr^3} + \beta^{ps}(r)\frac{d^2(\cdot)}{dr^2} + \gamma^{ps}(r)\frac{d(\cdot)}{dr} + \delta^{ps}(r)(\cdot)$ with $\alpha^{ps} = \frac{2}{r} - \frac{2}{E}\frac{dE}{dr}$, $\beta^{ps} = -\frac{1}{E}\frac{d^2E}{dr^2} + \frac{2}{E^2}\left(\frac{dE}{dr}\right)^2 + \frac{\nu}{rE}\frac{dE}{dr} - \frac{2}{rE}\frac{dE}{dr} - \frac{9}{r^2}$, $\gamma^{ps} = \frac{\nu}{rE}\frac{d^2E}{dr^2} - \frac{2\nu}{rE^2}\left(\frac{dE}{dr}\right)^2 + \frac{9}{r^2E}\frac{dE}{dr} + \frac{9}{r^3}$ and $\delta^{ps} = -\frac{4\nu}{r^2E}\frac{d^2E}{dr^2} + \frac{8\nu}{r^2E^2}\left(\frac{dE}{dr}\right)^2 - \frac{12}{r^3E}\frac{dE}{dr}$.

Relation (11) is a fourth-order linear differential equation with variable coefficients, and it is solved by considering the following boundary conditions

$$\begin{aligned} &\sigma_r^{ps}(a,\theta) = 0\,, \\ &\sigma_{r\theta}^{ps}(a,\theta) = 0\,, \\ &\lim_{r\to\infty} \sigma_r^{ps}(r,\theta) = \frac{\sigma_0}{2}\cos 2\theta\,, \\ &\lim_{r\to\infty} \sigma_{r\theta}^{ps}(r,\theta) = -\frac{\sigma_0}{2}\sin 2\theta\,. \end{aligned} \qquad (12a\text{-}d)$$

The set of the above equations for the two sub-problems can be found in [15].

3. The optimization problem: Motivation and formulation

Stresses for the case of a homogeneous infinite plate with a circular hole and subject to a uniaxial traction can be determined by taking Young's modulus as constant in the aforementioned equations, leading to the well-known Kirsch stress field [44]

$$\begin{aligned} \sigma_r(r,\theta) &= \frac{\sigma_0}{2}\left(1 - \frac{a^2}{r^2}\right) + \frac{\sigma_0}{2}\left(1 + \frac{3a^4}{r^4} - \frac{4a^2}{r^2}\right)\cos 2\theta, \\ \sigma_\theta(r,\theta) &= \frac{\sigma_0}{2}\left(1 + \frac{a^2}{r^2}\right) - \frac{\sigma_0}{2}\left(1 + \frac{3a^4}{r^4}\right)\cos 2\theta, \\ \sigma_{r\theta}(r,\theta) &= -\frac{\sigma_0}{2}\left(1 - \frac{3a^4}{r^4} + \frac{2a^2}{r^2}\right)\sin 2\theta. \end{aligned} \qquad (13a\text{-}c)$$

It can be easily shown that the SCF at the rim of the circular hole is identically 3 by taking the limit of Eq. (13b) for $r \to a$ and $\theta = \pi/2$ and dividing by σ_0. This value has been drastically reduced by replacing homogeneous materials by functionally graded ones. For instance, according to [15], one can reduce the SCF at the rim of the hole by suitably varying the two heterogeneity factors n and β, linked to the Young's modulus through the relation

$$E(r) = E_\infty \left[1 + \beta \left(\frac{r}{a}\right)^n\right], \tag{14}$$

where $E_\infty = \lim\limits_{r\to\infty} E(r)$, $-1 < \beta < 1$ and $n < 0$ (Figure 2a shows the radial distribution of Young's modulus for $n = -5$ and for different instances of $\beta < 0$). A similar relation for Poisson's ratio has been employed with different heterogeneity factors, but it was found that it does not affect stresses significantly (for this problem, the order of discrepancy is less than 1%). Expressions for the associated stress field on MN are lengthy and therefore omitted in this article, but represented in a graphical form in Figure 2b (see [15]). It is important to notice that although the SCF may arbitrarily tend to 0^+, an increase of the hoop stress occurs elsewhere along the radius, say at $r = \tilde{a}$. Denoting here after by $\breve{\sigma}_\theta(r)$ the hoop stress along the vertical line MN, such inevitable increase takes place as the improper integral $\lim\limits_{r\to\infty} \int_a^r \breve{\sigma}_\theta(t)\, dt$, resulting from the equilibrium between the applied load and occurring hoop stresses, is constant regardless of the Young's modulus distribution.

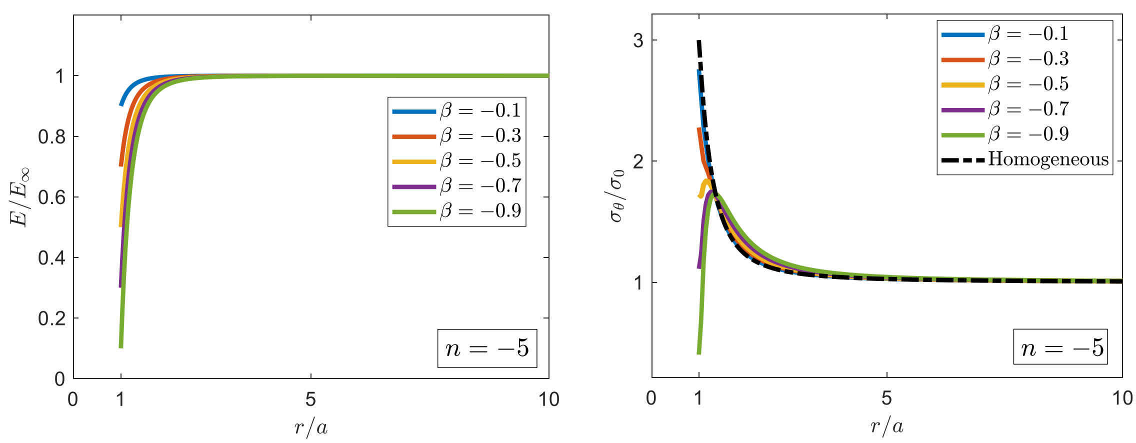

(a) (b)

Fig. 2: (a) Variation of Young's modulus with r/a for $n = -5$ and for different values of $\beta < 0$. (b) The associated hoop stresses (solid lines) alongside with Kirsch solution (dashed line) on the vertical line MN. Stresses associated with other Young's modulus distributions are addressed in [15].

Thus, the optimum scenario, for the Young's modulus distribution (14), occurs when the heterogeneity factors lead to a constant hoop stress for $r \in [a, \tilde{a}]$, or, *lato sensu*, to a hoop stress whose standard deviation (or statistical variation) is as minimum as possible. This problem has not been addressed in [15], as authors focused on finding analytical solutions for stresses. The formulation of the SCF minimization problem without remarkably increasing the hoop stress along the radius has been addressed in [16], albeit for a homogeneous isotropic infinite plate endowed with a functionally graded ring of radius $b > a$, where the Young's modulus distribution is given by

$$E(r) = E_b \left(\frac{r}{b}\right)^m , \tag{15}$$

where E_b is the Young's modulus at $r = b$ and m is a real positive number playing the role of the heterogeneity factor (see Figure 3a where different Young's modulus distributions are shown).

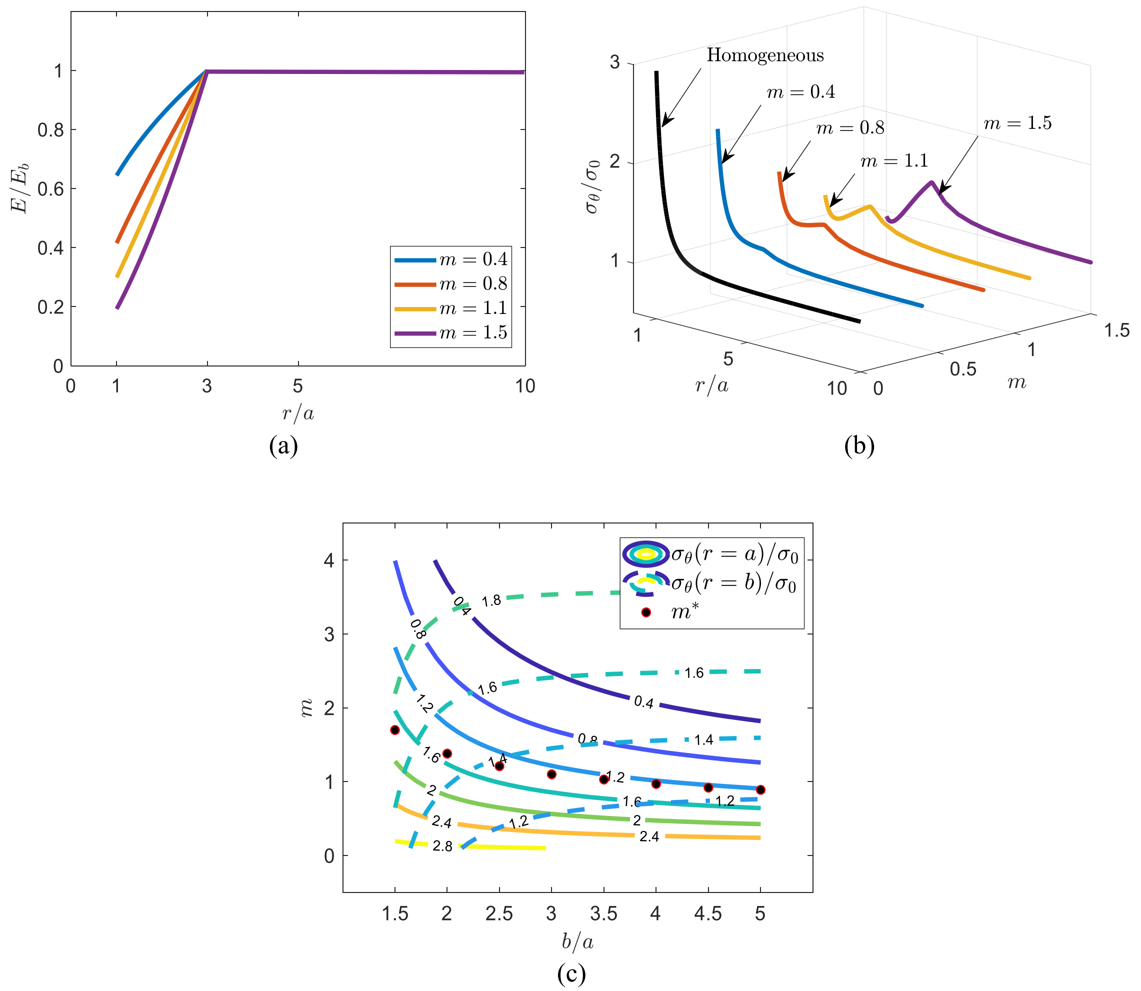

Fig. 3: (a) Variation of Young's modulus with $b/a = 3$ and for different values of $m > 0$. (b) The associated hoop stresses on the vertical line MN alongside with the Kirsch solution. (c) Contour levels for SCFs at the rim of the circular hole (solid contours), the interface between the ring and the homogeneous media (dashed contours) and best homogeneous factors m^* (scatter points). Stresses associated with other ring radii are addressed in [16].

Also here, Poisson's ratio ν is assumed constant and equal to the value of the homogeneous medium. Unlike [15], however, the author not only discussed the analytical tractability of the stress field (whose expression is omitted in this article), but also gave hints on the choice of the best heterogeneity factor for the optimum distribution for the hoop stress throughout the plate. In other words, the author showed that, regardless of the ring geometry, there exists a value of m, say m^*, such that the hoop stress assumes the same value at $r = a$ and $r = b$ and less elsewhere, provided that the search for m^* takes place in the range [16]

$$0 < m^* \leq \frac{8(2-\sqrt{3})}{\nu - 7 + 4\sqrt{3}} \tag{16}$$

to avoid complex values for the stress field. Figure 3b shows the normalized hoop stresses along the vertical line MN for different instances of m and for $b/a = 3$ and compared with (13b). It is shown that the value of the best heterogeneity factor is approximately $m^* = 1.1$ [16]. For completeness, it is desired to study the dependence of m^* on the geometry of the ring. A possible way is to compute contour levels for the SCFs at the rim of the circular hole and at the interface of the ring with the homogeneous medium for a range of admissible m, in the sense of the upper and lower limits given by Eq. (16), and for different values of b/a. By construction, the intersection of the two contour levels thus helps the reader identify the best heterogeneity factors m^* for fixed values of the ring geometry b/a. This practical chart is shown in Figure 3c, where the values for m^* are represented by scatter points. It is worth noting that the optimum heterogeneity factor monotonically decreases as b/a increases, namely a stiffer material at the circular hole is needed to compensate for the increase in the ring radius.

Based on the aforementioned considerations, an optimization problem in which the distribution of Young's modulus is sought for the minimization of the SCF arises. In order to avoid stress peaks along the radial direction the goal of minimizing the SCF can be replaced by the minimization of the maximum hoop stress along the line MN (see Figure 1a), namely

$$\check{\sigma}_{\theta,\max} = \max_{r \geq a} \check{\sigma}_\theta\,(r)\,, \tag{17}$$

as the hoop stress, for any (axisymmetric) Young's modulus variation, is expected to reach its peak only along this line. Hence, the optimization problem consists in finding the

Young's modulus distribution (or, through Eq. (1), the volume fraction) along the radial direction such that the maximum value for the hoop stress along MN reaches its minimum value, namely

Problem 1. $\min_{V(r)}$ (17) ,

s.t. (1) ,

(5a-c) ,

(6a-c) ,

(11) ,

(12a-d) .

Consequently, Problem 1 does not assume any a priori functional form of Young's modulus along the radial direction.

In the parlance of optimization theory, Problem 1 is referred to as *dynamic* optimization problem, namely an optimization problem whose decision variables are unknown piecewise continuous functions living in a certain domain, and constraints are differential relations. Solution to Problem 1 is cumbersome from the analytical viewpoint, requiring one to resort to numerical methods. Among all, the so-called direct transcription approach is used, which helps convert the dynamic optimization problem into a nonlinear programming (NLP) problem, namely to an optimization problem whose decision variables are collected in a finite-dimensional vector and constraints consist in equality or inequality algebraic relations. The conversion of algebraic and differential constraints (5a-c)-(6a-c) and (11)-(12a-d) into algebraic ones can be carried out by classic numerical methods in mechanics such as the finite- element, volume, or difference methods. In this article, the latter method is employed due to the simplicity of the boundary conditions of the problem under consideration. Hence, the governing equations for the biaxial and pure shear problems are solved by the finite difference method, which is recalled in the next Section for the sake of a self-contained work. Subsequently, to validate the finite difference code, an infinite functionally graded plate with a prefixed Young's modulus distribution of the form (14) is numerically solved and compared to analytical solutions in [15].

4. Direct transcription approach

Hereinafter, the discretization scheme and matrices assembly are performed along the vertical line MN (i.e., with $\theta = \pi/2$) up to a limit radius A sufficiently large (namely $a \ll A < \infty$). Denoting by K the number of (equally distant) discretization points r_k ($k = 1,2,\dots,K$) and letting $r_1 = a$ and $r_k = A$, Table 1 lists the finite difference expressions employed to substitute the different derivatives appearing in the governing equations at the generic node r_k, where Ψ generically represents the unknown variable, i.e., either σ_r^{bx} in Eq. (6a) or g in Eq. (11), and $\Delta r = \frac{A-a}{K-1}$ denotes the radial step. Finite difference approximation terms have been chosen to guarantee a second-order accuracy.

Tab. 1: Second-order accuracy expressions for the finite difference terms for the approximation of the different derivatives [45]. Here, Ψ_k denotes the value of Ψ at the generic node r_k.

Node	Derivative	Approximation
First	Forward 1st derivative	$\frac{d\Psi}{dr} \approx \frac{-\Psi_3+4\Psi_2-3\Psi_1}{2\Delta r}$
	Forward 2nd derivative	$\frac{d^2\Psi}{dr^2} \approx \frac{2\Psi_1-5\Psi_2+4\Psi_3-\Psi_4}{\Delta r^2}$
Last	Backward 1st derivative	$\frac{d\Psi}{dr} \approx \frac{\Psi_{K-2}-4\Psi_{K-1}+3\Psi_K}{2\Delta r}$
	Backward 2nd derivative	$\frac{d^2\Psi}{dr^2} \approx \frac{-\Psi_{K-3}+4\Psi_{K-2}-5\Psi_{K-1}+2\Psi_K}{\Delta r^2}$
Intermediate	Central 1st derivative	$\frac{d\Psi}{dr} \approx \frac{\Psi_{k+1}-\Psi_{k-1}}{2\Delta r}$
	Central 2nd derivative	$\frac{d^2\Psi}{dr^2} \approx \frac{\Psi_{k+1}-2\Psi_k+\Psi_{k-1}}{\Delta r^2}$
	Central 3rd derivative	$\frac{d^3\Psi}{dr^3} \approx \frac{\Psi_{k+2}-2\Psi_{k+1}+2\Psi_{k-1}-\Psi_{k-2}}{2\Delta r^3}$
	Central 4th derivative	$\frac{d^4\Psi}{dr^4} \approx \frac{\Psi_{k+2}-4\Psi_{k+1}+6\Psi_k-4\Psi_{k-1}+\Psi_{k-2}}{\Delta r^4}$

Firstly, the finite difference method is applied to Eqs. (6a-c). Taking into account the different expressions in Table 1, and after some algebra, Eq. (6a) can be rewritten as the following system of $K-2$ algebraic equations

$$\begin{aligned} &\sigma_{r\,k+1}^{bx}\left(2+\Delta r\,\alpha_k^{bx}\right)+\sigma_{r\,k}^{bx}\left(-4+2\Delta r^2\,\beta_k^{bx}\right) \\ &\qquad +\sigma_{r\,k-1}^{bx}\left(2-\Delta r\,\alpha_k^{bx}\right)=0\,, \end{aligned} \qquad k=2,3,\dots,K-1 \tag{18}$$

while boundary conditions (6b,c) are simply replaced by their approximations

$$\begin{aligned} \sigma_{r\,1}^{bx}&=0\,,\\ \sigma_{r\,K}^{bx}&=\frac{\sigma_0}{2}\,. \end{aligned} \tag{19a,b}$$

Equations (18)-(19a,b) can thus be written in the matrix form

$$\mathbf{A}\,\mathbf{\Sigma}=\mathbf{m}\,, \tag{20}$$

where $\mathbf{A}\in\mathbb{R}^{K\times K}$ is a square tridiagonal matrix, $\mathbf{\Sigma}\in\mathbb{R}^{K}$ is a column vector whose elements are the variables $\sigma_{r\,1}^{bx},\sigma_{r\,2}^{bx},\dots,\sigma_{r\,K}^{bx}$ and $\mathbf{m}\in\mathbb{R}^{K}$ is a column vector whose first $K-1$ elements are zeros and the last one is $\sigma_0/2$.

The same considerations can be taken into account for Eqs. (11)-(12a-d). Equation (11) can be rewritten as the following system of $K-4$ algebraic equations

$$\begin{aligned} &g_{k+2}\left(2+\Delta r\,\alpha_k^{ps}\right)+g_{k+1}\left(-8-2\Delta r\,\alpha_k^{ps}+2\Delta r^2\,\beta_k^{ps}+\Delta r^3\,\gamma_k^{ps}\right)\\ &\qquad +g_k\left(12-4\Delta r^2\,\beta_k^{ps}+2\Delta r^4\,\delta_k^{ps}\right)\\ &\qquad +g_{k-1}\left(-8+2\Delta r\,\alpha_k^{ps}+2\Delta r^2\,\beta_k^{ps}-\Delta r^3\,\gamma_k^{ps}\right)\\ &\qquad +g_{k-2}\left(2-\Delta r\,\alpha_k^{ps}\right)=0\,. \end{aligned} \qquad k=3,4,\dots,K-2 \tag{21}$$

Also here, the terms α_k^{ps}, β_k^{ps}, γ_k^{ps} and δ_k^{ps} can be derived by using the derivative approximations in Table 1 of their expressions. Finally, boundary conditions (12a-d), with the aid of Eqs. (10a-c), can be approximated as follows

$$\begin{aligned} &\frac{1}{a}\frac{g_3+4g_2-3g_1}{2\Delta r}-\frac{4g_1}{a^2}=0\,,\\ &\frac{1}{a}\frac{g_3+4g_2-3g_1}{2\Delta r}-\frac{g_1}{a^2}=0\,,\\ &\frac{1}{A}\frac{g_{K-2}-4g_{K-1}+3g_K}{2\Delta r}-\frac{4g_K}{A^2}=\frac{\sigma_0}{2}\,,\\ &\frac{1}{A}\frac{g_{K-2}-4g_{K-1}+3g_K}{2\Delta r}-\frac{4g_K}{A^2}=-\frac{\sigma_0}{4}\,, \end{aligned} \tag{22a-d}$$

respectively, where the far-field boundary conditions have been evaluated at the last discretization point $r_K = A \gg a = r_1$. The resulting system of equations can be recast in the matrix form

$$\mathbf{B}\,\mathbf{\Gamma} = \mathbf{n}\,, \tag{23}$$

where $\mathbf{B} \in \mathbb{R}^{K\times K}$ is the a square pentadiagonal matrix, $\mathbf{\Gamma} \in \mathbb{R}^{K}$ is a column vector whose elements are the variables $g_1, g_2, \dots, g_K$ and $\mathbf{n} \in \mathbb{R}^{K}$ is a column vector whose first $K-2$ elements are zeros and the last two are $\sigma_0/2$ and $-\sigma_0/4$, respectively. Elastic uniform biaxial and pure shear stresses are embedded into Eqs. (20) and (23), respectively, whose solutions are given by

$$\mathbf{\Sigma} = \mathrm{inv}(\mathbf{A})\,\mathbf{m}\,, \tag{24}$$

and

$$\mathbf{\Gamma} = \mathrm{inv}(\mathbf{B})\,\mathbf{n}\,. \tag{25}$$

where $\mathrm{inv}(\cdot)$ is the inverse operator for square matrices.

The finite difference method has been implemented successfully for the computation of stresses arising in functionally graded bodies in several circumstances, e.g., [46,47]. Nevertheless, before proceeding with the solution of the optimization problem, an example showing the validation of the method is necessary. Analytical solutions for the stresses are thus borrowed from the literature and compared to the numerical results. Among others, closed-form solutions derived in [15] are taken into account, where mechanical properties are described by the general power-law (14) for $\beta = \pm 0.9$ and $n = -5$. Figure 4a shows the analytical solutions for the radial and hoop stresses (solid lines) in the plate along MN and the numerical solutions (scatter points) by means of the finite difference method. A mesh convergence study has been carried out for the Young's modulus variation (14) adopted in [15] with $\beta = \pm 0.9$ and $n = -5$. In particular, it was found that the maximum values of the occurring stresses satisfy the convergence criterion $\sigma_{j,\max}^{(K_{i+1})} - \sigma_{j,\max}^{(K_i)} \leq 10^{-2}$MPa beyond $K = 300$, being i and $i+1$ two numerical forecasts employing K_i and K_{i+1} nodes, respectively, and $j = r, \theta$ (see Figure 4b).

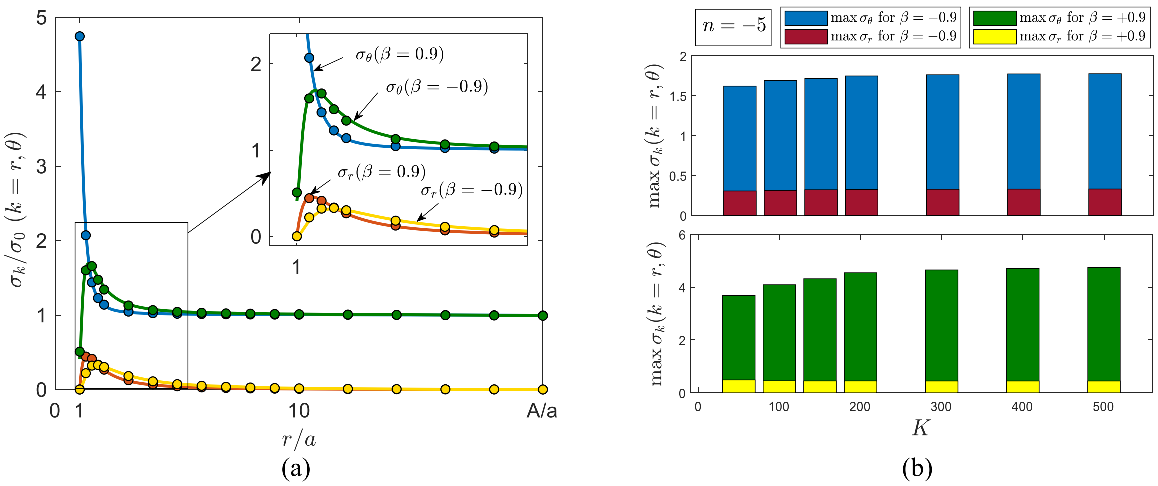

Fig. 4: (a) Analytical (solid lines) versus numerical (scatter points) solutions for the normalized radial and hoop stresses along the vertical line MN associated with the Young's modulus distribution in Eq. (14) with $\beta = \pm 0.9$ and $n = -5$. The parameters adopted for the simulation are $\nu = 0.3$ and $A/a = 20$. (b) Convergence study for the maximum radial and hoop stresses as functions of K.

Eventually, the maximum operator appearing in Eq. (17) is replaced by its p-norm approximation (where p is an even number greater than or equal 2), given by

$$\sigma_{\theta,\max} \approx \left(\int_a^A \breve{\sigma}_\theta(r)^p\, dr\right)^{\frac{1}{p}} \tag{26}$$

and evaluated by means of the well-known trapezoidal rule, namely

$$\breve{\sigma}_{\theta,\max} \approx \left[\Delta r\left(\breve{\sigma}_\theta(a)^p + \breve{\sigma}_\theta(A)^p + \sum_{i=2}^{K-1} \breve{\sigma}_\theta(r_i)^p\right)\right]^{\frac{1}{p}}. \tag{27}$$

Thus, Problem 1 can be transcribed into the following NLP problem.

Problem 2. $\min_{\mathbf{V}\in\mathbb{R}^K}$ $\breve{\sigma}_{\theta,\max} \approx \left[\Delta r\left(\breve{\sigma}_{\theta\,1}^p + \breve{\sigma}_{\theta\,K}^p + \sum_{i=2}^{K-1} \breve{\sigma}_{\theta\,i}^p\right)\right]^{\frac{1}{p}}$

s.t.

$$E_j = \tilde{E}_1(1 - V_j) + \tilde{E}_2 V_j\,, \qquad j = 1, 2, \dots, K$$

$$\textstyle\sum_{i=1}^K A_{ji}\, \sigma_{r\,i}^{bx} - m_j = 0\,, \qquad j = 1, 2, \dots, K$$

$$\textstyle\sum_{i=1}^K B_{ji}\, g_i - n_j = 0\,, \qquad j = 1, 2, \dots, K$$

$$\breve{\sigma}_{\theta\,j} - \sigma_{r\,j}^{bx} + r_j \frac{\sigma_{r\,j+1}^{bx} - \sigma_{r\,j-1}^{bx}}{2\Delta r} - \frac{g_{j+1} - 2g_j + g_{j-1}}{\Delta r^2} = 0\,, \qquad j = 2, 3, \dots, K-1$$

$$\breve{\sigma}_{\theta\,1} - \sigma_{r\,1}^{bx} + a\frac{-3\sigma_{r\,1}^{bx} + 4\sigma_{r\,2}^{bx} - \sigma_{r\,3}^{bx}}{2\Delta r} - \frac{2g_1 - 5g_2 + 4g_3 - g_4}{\Delta r^2} = 0\,,$$

$$\breve{\sigma}_{\theta\,K} - \sigma_{r\,K}^{bx} + A\frac{\sigma_{r\,K-2}^{bx} - 4\sigma_{r\,K-1}^{bx} + 3\sigma_{r\,K}^{bx}}{2\Delta r} - \frac{-g_{K-3} + 4g_{K-2} - 5g_{K-1} + 2g_K}{\Delta r^2} = 0\,,$$

where the volume fraction has been replaced by a finite-dimensional vector $\mathbf{V} = (V_1, V_2, \dots, V_K) \in \mathbb{R}^K$, linked to Young's modulus through Eq. (1), being fixed the stiffness ratio $\tilde{E}_2/\tilde{E}_1$ and the exponent p for the objective function evaluation. The vector of the decision variables of the NLP problem consists of the K discrete variables $V_1, V_2, \dots, V_K$. The constraints are the discrete equations for the elastic problems (6a-c) and (11)-(12a-d). The optimal solution therefore yields the optimal variation of the volume fraction and the corresponding stress behavior throughout the plate.

5. Results and discussion

In this Section, numerical optimal solutions for Problem 2 are illustrated and discussed. Hereinafter, the exponent p was taken to be equal to 200 (higher values generally lead to results too large to represent as conventional floating-point values during the iteration process), which yields a good approximation of the maximum hoop stress associated with the optimal solution, as confirmed by numerical results below. A gradient-based solver has been employed to numerically compute the optimal decision variable such that the maximum hoop stress reaches its minimum value. The algorithm used in this study is the well-known sequential quadratic programming algorithm [48]. Termination tolerances on both the function value as well as on the first-order condition for optimality have been imposed as 10^{-6}. In the light of conclusions made in [49], a linear volume fraction has been chosen as an initial guess and the numerical optimal solution has been sought iteratively.

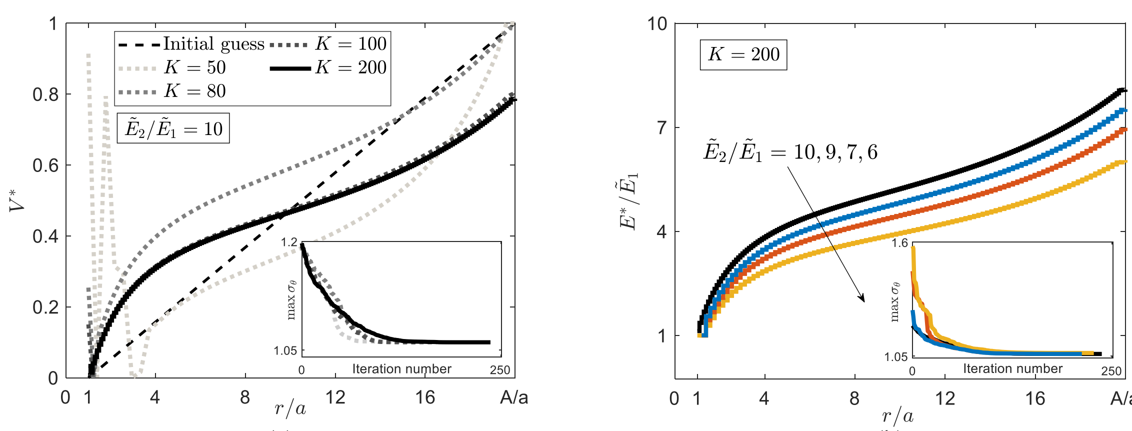

(a) (b)

Fig. 5: (a) The linear initial guess (dashed line) as well as optimal numerical solutions (dotted and solid lines) for the volume fraction as K increases considering $E_2/E_1 = 10$. (b) Optimal solutions for the Young's modulus distribution considering different stiffness ratios. Numerical forecasts have been performed with $p = 200$ and $A/a = 20$. The history of the iterations is also reported in the lower-right angle of each figure.

For the sake of comparison with the result obtained in [15], a first simulation has been performed with a stiffness ratio $\tilde{E}_2/\tilde{E}_1 = 10$. The initial target is therefore to compare numerical results with the stress performance associated with the Young's modulus distribution obtained with $\beta = -0.9$ and $n = -5$ (see Figures 2a,b or 4). Figure 5a shows the initial guess (dashed line) and numerical optimal volume fractions with the same load and geometrical parameters as those employed for the validation example. More precisely, successive numerical solutions were obtained for increasing K values (dotted lines) until a prefixed convergence criterion between consecutive optimal solutions is achieved. In particular, the considered optimal solution ($K = 200$, solid line) was chosen instead of another ones associated with lower nodes (e.g., $K = 100$) as the norm of their difference is less than 10^{-2}. It is worth noting that the optimal volume fraction increases throughout the radial direction, indicating the optimality of adopting a softer material at the rim of the circular hole. This finding is in agreement with the literature reporting enhancement studies for the SCF for plates with circular holes (see, e.g., [10]). The resulting optimal Young's modulus distribution is following a sort of sigmoid function around the linear distribution. Moreover, the optimal material distribution does not necessarily assume, as base materials, the functionally graded material constituents at the boundaries of the plate. Similar forecasts have been performed for different stiffness ratios $\tilde{E}_2/\tilde{E}_1$, leading to the same conclusion (see Figure 5b).

To assess the stress performance of the optimal solution, the associated elastic hoop, radial and shear stresses are respectively illustrated in Figures 6a,b,c (dotted lines). It is worth appreciating that the hoop stress is uniform throughout the plate and free of stress peaks, yielding a plateaued stress behavior and thus making the stress concentration vanish throughout the radial domain. Moreover, the radial and shear stresses obey the boundary conditions of the problem. It is worth noting that the optimization output is the same if the uniaxial load direction is rotated by $\pi/2$, provided that the optimization problem is formulated on the line associated with $\theta = 0$. To further assess the correctness of the stress field obtained by the optimal Young's modulus distribution, a finite element (FE) forecast was carried out by a commercial software (ANSYS Mechanical APDL 2022 R1). Due to symmetrical load and geometrical considerations, the geometrical domain consists of the quarter of the plate and is discretized by means of second-order quadrilateral plane stress elements (PLANE 183). Necessary symmetric boundary conditions and the uniaxial load have been suitably applied to the model. The radial direction has been discretized into 200 radial strips (the same discretization points used in the transcription procedure), each of which is isotropic and homogeneous and has the same mechanical properties. Adjacent layers present different properties such that the resulting piecewise constant variation approximates the optimal Young's modulus distribution displayed in Figure 5b. The FE stress behavior has been represented by scatter points, showing a remarkable fit with the optimization solver outputs, compared to the material modeling simplifications necessary for the FE forecast, and confirming the uniformity of the hoop stress on the line MN. Furthermore, a comparison between stresses obtained by the present approach alongside with those analytically derived in [15] (associated with $\beta = -0.9$ and $n = -5$) and in [16] for two different ring geometries ($b/a = 3$ and 5) is made (see solid lines). It is clear that the present approach leads to Young's modulus distributions (sigmoid-like curves) associated with the most uniform hoop stress (and consequently the minimum peak hoop stress) throughout the plate.

6. Conclusions

The optimization of the volume fraction distribution to minimize peak hoop stresses in functionally graded infinite plates with a circular hole and subjected to uniaxial traction is numerically addressed. The optimization problem has been stated and formulated as a dynamic optimization problem, where the variation of the decision variable, namely the volume fraction and consequently the Young's modulus through the rule of mixture, is unknown beforehand and not limited to specified functions along the radial direction. The problem has been divided into two sub-problems, i.e., occurring stresses have been assumed as the superposition of those resulting from the biaxial and from the pure shear deformations. Optimality conditions for the best distribution of the volume fraction could not be solved analytically, hence numerical methods were necessary.

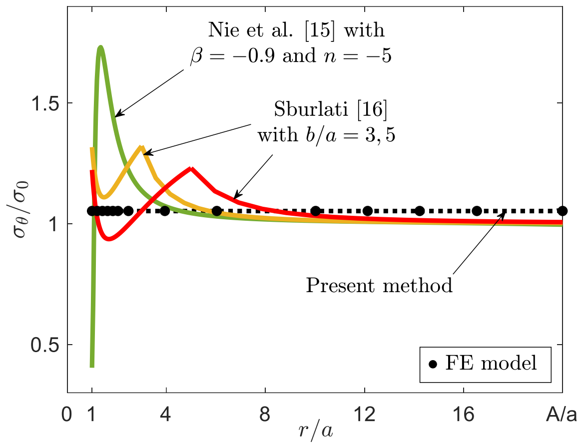

(a)

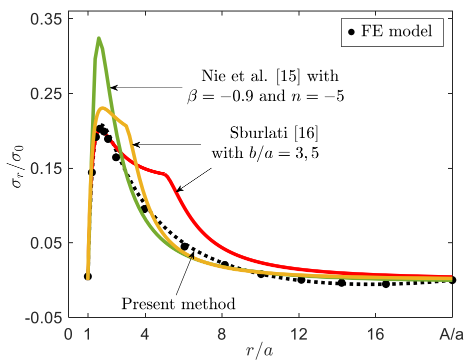

(b)

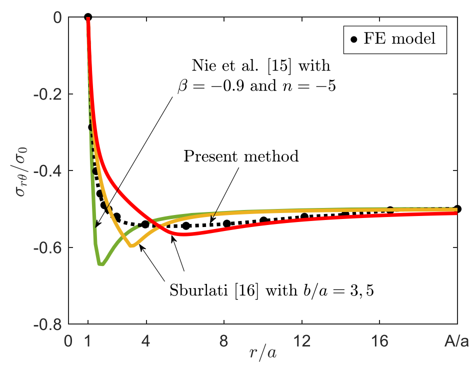

(c)

Fig. 6 Stresses associated with the optimal numerical solution (dotted lines) and finite element results (scatter points). (a) Hoop and (b) radial stresses along the vertical line MN and the (c) shear stress along $\theta = \pi/4$. Comparison between optimized stresses with results in literature (solid lines) [15,16].

The transcription procedure consisted in approximating the peak stress by the trapezoidal rule and converting the differential equations accounting for the elastic problem into two systems of algebraic equations describing the two sub-problems by means of the finite difference method due to the simplicity of the employed boundary conditions which permitted the solution with reduced computational costs. The obtained numerical solutions for the Young's modulus follow a sigmoidal behavior. The associated hoop stress revealed uniform along the radius and has been validated by the finite element method.

The Young's modulus distribution has been assumed to follow the rule of mixture; however, other models for the effective Young's modulus can be fitted in the same framework. The present article can be considered as a preliminary study whose results can be further extended as follows. For instance, other geometrical discontinuities such as elliptic or rounded-square holes can be taken into account, provided that the transcription of the differential elastic equations into algebraic equations is replaced by a suitable finite element approach.

References

[1] E.G. Kirsch. Die Theorie der Elastizität und die Bedürfnisse der Festigkeitslehre. *Zeitschrift des Vereines deutscher Ingenieure* **42**, pp. 797-807 (1898).

[2] R.D.B. Sevenois, S. Koussios. Analytic Methods for Stress Analysis of Two-Dimensional Flat Anisotropic Plates with Notches: An Overview. *Applied Mechanics Reviews* **66(6)**, 060802 (2014).

[3] S. Anoop Kumar, R. Rajesh, S Pugazhendhi. A review of stress concentration studies on fibre composite panels with holes/cutouts. *Proceedings of the Institution of Mechanical Engineers, Part L: Journal of Materials: Design and Applications* **234 (11)**, pp.1461-1472 (2020).

[4] B.G. Korenev. Punch lying on as elastic half-space whose modulus of elasticity is a function of the depth. *Doklady Akademii Nauk* **112**, pp. 823-826 (1957).

[5] G.I. Popov. Bending of an unbounded plate supported by an elastic half-space with a modulus of elasticity varying with depth. *Journal of Applied Mathematics and Mechanics* **23 (6)**, pp. 1566-1573 (1959).

[6] R.E. Gibson. Some results concerning displacements and stresses in a non-homogeneous elastic half-space. *Geotechnique* **17(1)**, pp. 58-67 (1967).

[7] C.O. Horgan, A.M. Chan. The pressurized hollow cylinder or disk problem for functionally graded isotropic linearly elastic materials. *Journal of Elasticity* **55**, pp. 43-59 (1999).

[8] J.F. Durodola, O. Attia. Deformation and stresses in functionally graded rotating disks. *Composites Science and Technology* **60**, pp. 987-995 (2000).

[9] T. Singh, V.K. Gupta. Effect of anisotropy on steady state creep in functionally graded cylinder. *Composite Structures* **93**, pp. 747-758 (2011).

[10] D.V. Kubair, B. Bhanu-Chandar. Stress concentration factor due to a circular hole in functionally graded panels under uniaxial tension. *International Journal of Mechanical Sciences* **50**, pp.732-742 (2008).

[11] T.A. Enab. Stress concentration analysis in functionally graded plates with elliptic holes under biaxial loadings. *Ain Shams Engineering* **5**, pp. 839-850 (2014).

[12] M. Mohammadi, J.R. Dryden, L. Jiang. Stress concentration around a hole in a radially inhomogeneous plate. *International Journal of Solids and Structures* **48**, pp. 483-491 (2011).

[13] Q. Yang, C.F. Gao, W. Chen. Stress analysis of a functional graded material plate with a circular hole. *Archive of Applied Mechanics* **55(7)**, pp. 1263–1271 (2010).

[14] M. Kushwaha, P.K. Saini. An analytical approach to reduce the stress concentration around a circular hole in a functionally graded material plate under axial load. *Applied Mechanics and Materials* **592-594**, pp. 985-989 (2014).

[15] G.J. Nie, Z. Zhong, R.C. Batra. Material tailoring for reducing stress concentration factor at a circular hole in a functionally graded material (FGM) panel. *Composite Structures* **205**, pp. 49-57 (2018).

[16] R. Sburlati. Stress concentration factor due to a functionally graded ring around a hole in an isotropic plate. *International Journal of Solids and Structures* **50**, pp. 3649-3658 (2013).

[17] R. Sburlati, S.R. Atashipour, S.A. Atashipour. Reduction of the stress concentration factor in a homogeneous panel with hole by using a functionally graded layer. *Composite: Part B* **61**, pp. 99-109 (2014).

[18] S. Nikbakht, S. Kamarian, M. Shakeri. A review on optimization of composite structures Part II: Functionally graded materials. *Composite Structures* **214**, pp. 83–102 (2019).

[19] P. Nayak, A. Armani. Optimal Design of Functionally Graded Parts. *Metals* **12(8)**, 1335 (2022).

[20] A. Ghazanfari, M.C. Leu. Composition Optimization for Functionally Gradient Parts Considering Manufacturing Constraints. In: *Proceedings of the ASME 2014 International Manufacturing Science and Engineering Conference collocated with the JSME 2014 International Conference on Materials and Processing and the 42nd North American Manufacturing Research Conference*, Detroit, MI, USA, 9–13 June 2014.

[21] M. Jamshidi, J. Arghavani. Optimal design of two-dimensional porosity distribution in shear deformable functionally graded porous beams for stability analysis. *Thin-Walled Structures* **120**, pp. 81-90 (2017).

[22] H.M. Abo-Bakr, S.A. Mohamed, M.A. Eltaher. Weight optimization of axially functionally graded microbeams under buckling and vibration behaviors. *Mechanics Based Design in Structures and Machines* **51(1)**, pp. 213-342 (2020).

[23] A.W. Leissa, M. Vagins. The design of orthotropic materials for stress optimization. *International Journal of Solids and Structures* **14**, pp. 517–526 (1978).

[24] K. Tian, X. Ma, Z. Li, S. Lin, B. Wang, A.M. Waas. A multi-fidelity competitive sampling method for surrogate-based stacking sequence optimization of composite shells

with multiple cutouts. *International Journal of Solids and Structures* **193-194**, pp.1-12 (2020).

[25] A. Nouri, S. Astaraki. Optimization of Sound Transmission Loss through a Thin Functionally Graded Material Cylindrical Shell. *Shock and Vibration*, 814682 (2014).

[26] H.M.A. Abdalla, D. Casagrande, L. Moro. Thermo-mechanical analysis and optimization of functionally graded rotating disks. *Journal of Strain Analysis for Engineering Design* **55(5–6)**, pp. 159-171 (2020).

[27] A.M. Eldeeb, Y.M. Shabana, A. Elsawaf. Particle Swarm Optimization for the Thermoelastic Behaviors of Functionally Graded Rotating Nonuniform Thickness Sandwich Discs. *Arabian Journal for Science and Engineering* **48**, pp. 4067-4079 (2022).

[28] R. Madan, S. Bhowmick. Optimum FG Rotating Disk of Constant Mass: Lightweight and Economical Alternatives Based on Limit Angular Speed. *Iranian Journal of Science and Technology, Transactions of Mechanical Engineering* **47(3)**, pp. 1019-1033 (2023).

[29] Z.W. Wang, Q. Zhang, L.Z. Xia, J.T. Wu, P.Q. Liu. Stress analysis and parameter optimization of an FGM pressure vessel subjected to thermo-mechanical loadings. *Procedia Engineering* **130**, pp. 374-389 (2015).

[30] Z.W. Wang, Q. Zhang, L.Z. Xia, J.T. Wu, P.Q. Liu. Thermomechanical analysis of pressure vessels with functionally graded material coating. *Journal of Pressure Vessel Technology* **138(1)**, 011205 (2016).

[31] M. Khorsand, Y. Tang. Thermal analysis and electro-elastic response of multilayered spherical vessels. *International Journal of Pressure Vessels and Piping* **171**, pp. 194-206 (2019).

[32] R. Chiba, Y. Sugano. Optimisation of material composition of functionally graded materials based on multiscale thermoelastic analysis. *Acta Mechanica* **223**, pp. 891-909 (2012).

[33] Q.X. Lieu, J. Lee. Modeling and optimization of functionally graded plates under thermo-mechanical load using isogeometric analysis and adaptive hybrid evolutionary firefly algorithm. *Composite Structures* **179**, pp. 89-106 (2017).

[34] F. Moleiro, J. Madeira, E. Carrera, J.N. Reddy. Design optimization of functionally graded plates under thermo-mechanical loadings to minimize stress, deformation and mass. *Composite Structures* **245**, 112360 (2020).

[35] R.C. Batra. Material tailoring and universal relations for axisymmetric deformations of functionally graded rubberlike cylinders and spheres, *Mathematics and Mechanics of Solids* **16(7)**, pp. 729-738 (2011).

[36] J. Nie, Z. Zhong, R.C. Batra. Material tailoring for functionally graded hollow cylinders and spheres, *Composite Science and Technology* **71**, pp. 666-673 (2011).

[37] M. Carraturo, E. Rocca, E. Bonetti, D. Homberg, A. Reali, F. Auricchio. Graded-material design based on phase-field and topology optimization, *Computational Mechanics* **64**, pp. 1589-1600 (2019).

[38] T. Hu, Y. Wang, H. Zhang, H. Li, X. Ding, K. Izui, S. Nishiwki. Topology optimization of coated structures with layer-wise graded lattice infill for maximizing the fundamental eigenfrequency. *Computers & Structures* **271**, 106861 (2022).

[39] H.M.A. Abdalla, D. Casagrande, F. De Bona. A Dynamic Programming Setting for Functionally Graded Thick-Walled Cylinders. *Materials* **13**, 3988 (2020).

[40] H.M.A. Abdalla, D. Casagrande. An Intrinsic Material Tailoring Approach for Functionally Graded Axisymmetric Hollow Bodies Under Plane Elasticity. *Journal of Elasticity* **144**, pp. 15-32 (2021).

[41] H.M.A. Abdalla, D. Boussaa, R. Sburlati, D. Casagrande. On the best volume fraction distributions for functionally graded cylinders, spheres and disks – A pseudospectral approach. *Composite Structures* **311**, 116784 (2023).

[42] Y. Zhou, Q. Lin, J. Hong, N. Yang. Optimal design of functionally graded material for stress concentration reduction. *Structures* **29**, pp. 561-569 (2021).

[43] Y. Miyamoto, W.A. Kaysser, B.H. Rabin, A. Kawasaki, R.G. Ford. *Functionally Graded Materials. Design, Processing and Applications.* London: Kluwer Academic (1999).

[44] S.P. Timoshenko, J.N. Goodier. *Theory of elasticity*. New York: McGraw Hill Higher Education (1970).

[45] J. Stoer, R. Burlisch. *Introduction to numerical analysis*. New York: Springer-Verlag (1980).

[46] Y. Zheng, H. Bahaloo, D. Mousanezhad, E. Mahdi, A. Vaziri, H. Nayeb-Hashemi. Stress analysis in functionally graded rotating disks with non-uniform thickness and variable angular velocity. *International Journal of Mechanical Sciences* **119**, pp. 283–93 (2016).

[47] A.M. Eldeeb, Y.M. Shabana, A. Elsawaf. Influences of angular deceleration on the thermoelastoplastic behaviors of nonuniform thickness multilayer FGM discs. *Composite Structures* **258**, 113092 (2021).

[48] S.S. Rao. *Optimization: theory and applications*. New Delhi: Wiley Eastern Ltd. (1978).

[49] H.M.A. Abdalla, D. Casagrande, F. De Bona. Analysis of Stress Concentration in Functionally Graded Plates with Linearly Increasing Young's Modulus. *Materials* **16**, 6882 (2023).

3D Dark-field X-ray Microscopy Intra-granular Dislocation Mapping in L-PBF AISI 316L Coupled with Texture Analysis and Computed Tomography

Alessandro Tognan[a,1,*], Can Yildirim[b], Marco Pelegatti[a], Aditya Shukla[b], Emanuele Vaglio[a], Federico Scalzo[a], Enrico Salvati[a,2,*]

[a]*Polytechnic Department of Engineering and Architecture, University of Udine, Via delle Scienze 206, Udine, 33100, Italy*

[b]*European Synchrotron Radiation Facility, 71 Avenue des Martyrs, Grenoble, 38043, France*

Abstract

Dislocations in Laser Powder Bed Fusion (L-PBF) AISI 316L closely relates to the material's stress state, response and damage at the inter- and intra-granular scales. Assessing the dislocation state and activity at these scales helps understand the material behaviour at larger length-scales. Nevertheless, most experimental studies have utilised surface or destructive methods, unable to probe the bulk non-invasively. We conduct the first Dark-Field X-ray Microscopy (DFXM) investigation to non-destructively assess the intra-granular dislocation density within an L-PBF AISI 316L grain in the bulk. The research unveiled sub-granular cells with orientation spread up to 4°, and intra-granular dislocation arrangements, signalling Type III Residual Stress (RS) in the bulk. Additional texture analysis indicated a predominant {110} orientation within the grain. Computed tomography on a miniaturised sample ($200 \times 200\,\mu m^2$ cross-section) enabled the statistical characterisation of its porosity. Pores were found close to the sample surface and geometrically regular, with sphericity mostly greater than 0.5.

Keywords: Dark field X-Ray Microscopy (DFXM); Laser Powder Bed Fusion (L-PBF); AISI 316L; Mosaicity; Dislocation Density.

December 23, 2025

Metal Additive Manufacturing (AM) has redefined the industrial fabrication scenario, offering numerous advantages and exceptional versatility over conventional manufacturing methods [1, 2]. Laser Powder Bed Fusion (L-PBF) is a renowned AM technique that currently handles a variety of metallic materials [3]. Among these, AISI 316L has gained considerable industrial relevance given its favourable cost-effective processability, thermo-mechanical properties, and chemical resistance [4]. Although the fabrication of L-PBF AISI 316L has reached a mature technological state, several unwanted features spanning multiple length scales affect the produced parts, thereby influencing their mechanical response.

The complex thermodynamic conditions within the AM melt pool give rise to defects of diverse morphologies, which reportedly scatters the resulting fatigue behaviour [5–7]. AM parts predominantly experience heat transfer along the build direction, leading to elongated columnar grains within intra-granular cells and, therefore, anisotropic microstructure and mechanical properties [8–11]. Depending on the AM process parameters, a fibre $\langle 100 \rangle$ or $\langle 110 \rangle$ crystallographic texture can be observed in L-PBF AISI 316L [12]. However, a random texture can be found for specific process parameters [13, 14].

Dislocation density strongly influences the mechanical properties of materials [15, 16]. Specifically, the dislocations in wall-like structures surrounding dislocation-free channels within the grains modulate plastic deformation mechanisms [17, 18]. This phenomenon results in higher yield stress than the conventionally manufactured counterpart [19], while leads to ultimate tensile strengths comparable to wrought materials without a pronounced reduction in elongation [20].

The build-up of dislocations and lattice mismatches also contributes to residual stress (RS) at the intra-granular level [21]. Moreover, local inhomogeneous of L-PBF thermal gradients triggers RS across the scales as in other conventional fabrication methods and joining

*Corresponding author
Email addresses: alessandro.tognan@uniud.it (Alessandro Tognan), can.yildirim@esrf.fr (Can Yildirim), marco.pelegatti@uniud.it (Marco Pelegatti), aditya.shukla@esrf.fr (Aditya Shukla), emanuele.vaglio@uniud.it (Emanuele Vaglio), federico.scalzo@uniud.it (Federico Scalzo), enrico.salvati@uniud.it (Enrico Salvati)
[1]ORCID: 0000-0001-8109-4034
[2]ORCID: 0000-0002-2883-0538

processes [22–24]. Despite targeted post-fabrication treatment [25], RS appears unavoidable. Hence, gaining an in-depth comprehension of RS arising from AM is of capital importance. For instance, the relief of AM-induced Type I (macro-scale) RS through post-fabrication treatments led to increased fatigue strength in the high-cycle fatigue regime [26]. Another study investigated the interplay between Type II (inter-granular) RS and dislocation density in as-built L-PBF AISI 316L samples. Therein, dislocations were also proven to produce tension-compression asymmetries in yield strength and work hardening [27]. The study principally provided experimental evidence of RS, without direct insights into dislocation distributions. Based on Electron Backscattered Diffraction (EBSD) investigations, some of the present authors demonstrated that RS play a marginal role in low-cycle fatigue regime, mainly due its relaxation, grain refinement, and dislocation rearrangement as the number of reversals increased [28]. L-PBF AISI 316L also exhibits a hierarchical sub-granular structure with a high density of dislocation, local plastic deformation at the intra-granular level, and therefore, Type III (intra-granular) RS [29–31].

Evidently, the experimental evaluation of dislocation density at the intra-granular would be pivotal to understand its interaction with RS formation in L-PBF AISI 316L, and therefore its mechanical response. Moreover, the above-discussed microstructural investigations were conducted through destructive experimental methods, e.g. EBSD. Since these techniques require sample or surface preparation, the experimental outcome can be biased [32]. To gain direct access to three-dimensional intra-granular information in the bulk in a non-invasive, one can resort to Dark-Field X-ray Microscopy (DFXM) [33]. This high-resolution, non-destructive 3D imaging technique employs full-field illumination and collects reflections from a selected crystallographic plane to reconstruct morphology, mosaicity, lattice strain, and stress within individual crystals [34, 35]. Notably, DFXM has permitted *intra-granular* characterisation of several metallic materials and alloys [36, 37], including *in-situ* experiments [38, 39]. Nevertheless, the literature currently lacks applications of DFXM to L-PBF AISI 316L.

In this work, we address the outstanding gaps outlined above by characterising, for the first time, the intra-granular orientation and dislocation density in an individual grain located in the bulk of an L-PBF AISI 316L sample via DFXM. The same method is also leveraged for texture mapping, whereas Computed Tomography (CT) is exploited to quantify the porosity of the samples, enabling a multi-modal characterisation of the bulk material.

A monolithic L-PBF AISI 316L specimen was fabricated by a Concept Laser M2 Cusing with parameters listed in Table 1. The specimen subsequently underwent Wire Electrical Discharge Machining to produce a batch of comb-like sheets, whose teeth are the sample for the experimental activity with dimensions $200 \times 200 \times 3500\,\mu m^3$, whose schematic is shown in Fig. 1(a). Specifically, labels `S1` and `S2` shall be used hereinafter to label to the two samples contained in the comb-like material used in this work. The experimental activity was entirely carried out at beamline `ID03` of the *European Synchrotron Radiation Facility* (Grenoble, France) [40].

Table 1: Process parameters used to fabricate the monolithic AISI 316L sample in this study. The same parameters were used by some of the present authors in a previous work [41], where the feedstock was also characterised.

Parameter	Value
Laser power	180 W
Scanning speed	600 mm/s
Spot diameter	120 µm
Hatch distance	105 µm
Layer thickness	25 µm

Sample `S1` was characterised by X-ray CT to assess the pore population. CT was performed on a near-field PCO detector coupled to a scintillator, mirror, and visible-light objective, yielding an effective pixel size of $0.65\,\mu m$. The detector was positioned approximately 100 mm downstream of the sample. A 17.0 keV beam box beam of approximately $1 \times 1\,mm^2$ was used to illuminate the sample. A total of 2000 projections were acquired over a 360° scan range. The CT reconstruction was carried out by `tomware` [42], the resulting image stack was segmented using the `3D ImageJ Suite` [43], and the segmented data were post-processed using custom `Python` scripts.

Sample `S1` was also probed to quantify the volume-averaged texture by collecting diffractions from a statistically representative population of grains within the illuminated gauge volume priorly CT-scanned. The analysis was performed at the same sample position as the CT without repositioning the specimen. The sample was illuminated using a box beam of approximately $300 \times 300\,\mu m^2$ at a photon energy of 55.12 keV. The detector geometry was calibrated using a Si single crystal and a Si powder standard. Diffraction images were recorded on a FReLoN detector (pixel size 47.3 µm) positioned 283 mm downstream of the sample. Texture data were acquired during an ω-rotation about the laboratory z-axis over 360 angular positions, with 0.5 s exposure per point and an effective angular integration of 1° per step. The recorded Debye–Scherrer rings were subsequently analysed to derive volume-averaged pole figures and the corresponding orientation distribution function (ODF) from the integrated diffraction intensities associated with the {111} and {200} reflection families [44]. The integration was done using `pyFAI` [45], whereas `MTEX` [46] was utilised for texture data post-processing and visualisation.

Sample `S2` was examined through DFXM, and Fig. 1(a) portrays the simplified schematic of the experimental setup. The setup provided an X-ray magnification of 13.8×, corresponding to an effective pixel size of 47 nm on the detector. DFXM local orientation (mosaicity) scans were performed around the 002 diffraction vector, i.e. by tilting the sample about Φ and χ at constant 2θ. A series of mosaicity scans were collected at successive sample heights to probe the variation along the grain. The scans were spaced by 2 µm in the vertical direction, thus effectively capturing a stack of virtual 2D slices through the diffracting 3D grain volume, whose reconstruction is presented in Fig. 1(b). Data processing and analysis were performed using `darfix` [47] and custom `MATLAB` routines, whereas the data post-processing was carried out with `Pyvista` and `Paraview` [48, 49]. Please note that the DFXM measurements reported in this work were conducted during a previous beamtime on a sample *extracted from the same* L-PBF *batch*, enabling direct comparison of intra-granular information with the present volume-averaged texture and porosity characterisation.

We start by showing the millimetre-scale X-ray CT results to visualise the overall morphology and porosity of the sample, before moving to texture and intragranular imaging. The

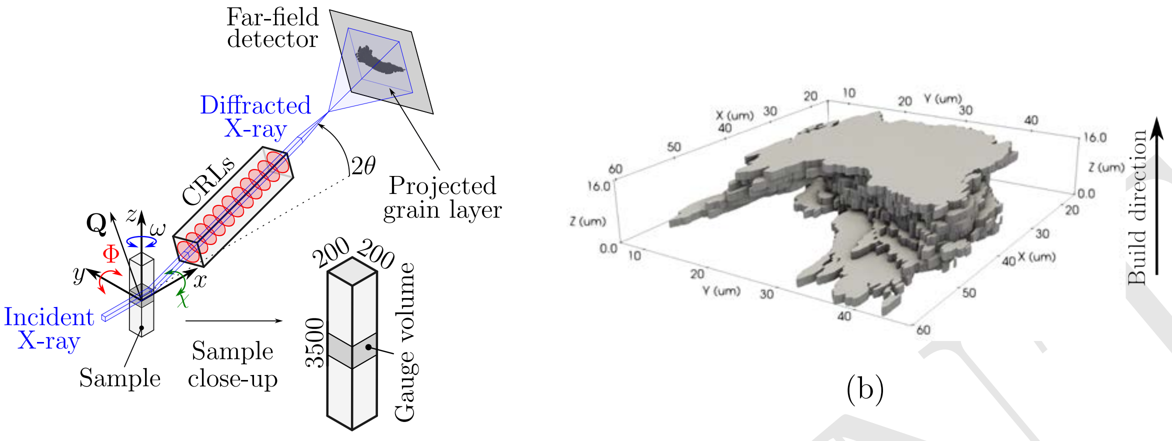

(a) (b)

Figure 1: (a) Schematic of the setup for DFXM employed for the present experiment, along with a close-up of the sample (dimensions are in µm), and the laboratory frame $\{x, y, z\}$. Slits were 1 mm open horizontally and 0.15 mm open vertically, thus giving an incident $1000 \times 0.5\,\mu m^2$ monochromatic beam with a photon energy of 19.2 keV. The beam was focused vertically onto the sample using Compound Refractive Lenses (CRLs) having 58 Be parabolic lenslets with 100 µm radius, forming a line beam with a height of approximately 500 nm at Full-width at Half-maximum (FWHM). A grain of interest was selected from the bulk material, and its 002 diffraction vector, **Q**, was aligned vertically so that it passed through the X-ray CRL objective composed of 87 two-dimensional Be with 50 µm radius. The diffracted beam through the objective was imaged using a PCO detector coupled with a scintillator located roughly at 5.25 m from the sample. (b) Reconstructed layer-wise morphology of the selected grain. The z-scale is magnified for aiding visualisation.

result of the segmentation of CT images for S2 is given in Fig. 2(a). The data post-processing indicates a total porosity of approximately 0.02%. Fig. 2(b)-(c) illustrates the distributions of pores' descriptors, including the minimum distance to the free surface, sphericity, and Murakami's $\sqrt{\text{area}}$ [50], which is frequently to define the fatigue crack driving force in diverse semi-empirical models [51]. Fig. 2(b) demonstrates that pores are mostly located close to the sample surface, whereas Fig. 2(c) shows that pore exhibits predominantly regular morphology ($S > 0.5$), which likely originated from gas entrapment or keyhole-related mechanisms [7, 52]. Fig. 2(d) illustrates the distribution of S as a function of $\sqrt{\text{area}}$, which is broadly consistent with findings by other authors [53, 54], although an exhaustive comparison is limited by the much larger gauge volumes used in those studies. Despite the small number of pores detected in the sample (17 in total), the pore shape and size distributions observed in this work aligns with those reported for similar ranges of S and $\sqrt{\text{area}}$.

From a structural integrity perspective, the characteristics of the detected pore population suggest a limited detrimental impact on the bulk performance of the material. In particular, the low overall porosity, the predominance of near-spherical morphologies, and the small values of $\sqrt{\text{area}}$ indicate a comparatively low potential stress concentration to irregular lack-of-fusion defects. Moreover, the proximity of the pores to the free surface may render them preferential sites for fatigue crack initiation under cyclic loading [50, 52, 55].

Next, we move to the volume-averaged diffraction mapping in order to establish the texture of the sample. Fig. 3 reports {110}, {200}, and {111} pole figures obtained from the ODF of sample `S2`. Despite the small investigated sample volume, a texture pattern can be observed. The {110} pole figure exhibits the maximum intensity near the z-direction. A slight difference, however, arises from the tilted sample orientation during the diffraction analysis, leading to ODF maximum intensities not perfectly aligned with the sample axes. Nevertheless, the pattern discovered over {110} pole figure matches the results by some of the authors of this work [28, 56], albeit obtained via EBSD and neutron diffraction. As concerns {200} pole figure, maximum intensities were found close to the x- and y-directions, which is corroborated by the EBSD analyses in [12]. Furthermore, the {111} pole figure reveals that the intensity maxima are distributed at off-axis positions, indicating that the dominant crystallographic orientations are inclined with respect to the principal sample directions. This observation is consistent with previous results from the literature [12, 28, 56].

We now zoom in on a grain of interest employing DFXM to reveal grain morphology and intra-granular dislocation structure. Specifically, the grain of interest was selected from the higher textured region in the {200} pole. The data herein are presented as 3D-stacked views. The reader can refer to Appendix A for the 2D representation of the data.

Fig. 4(a)-(c) illustrates the distribution of the local crystal orientation, namely CoM_Φ and CoM_χ. A qualitative inspection reveals pronounced local lattice tilts up to 4°. Alongside this, the histograms (Fig. 4(c)) displays considerable intra-granular orientation spread across the layers. Fig. 4(d) illustrates the mosaicity inferred from the CoMs over each grain layer,

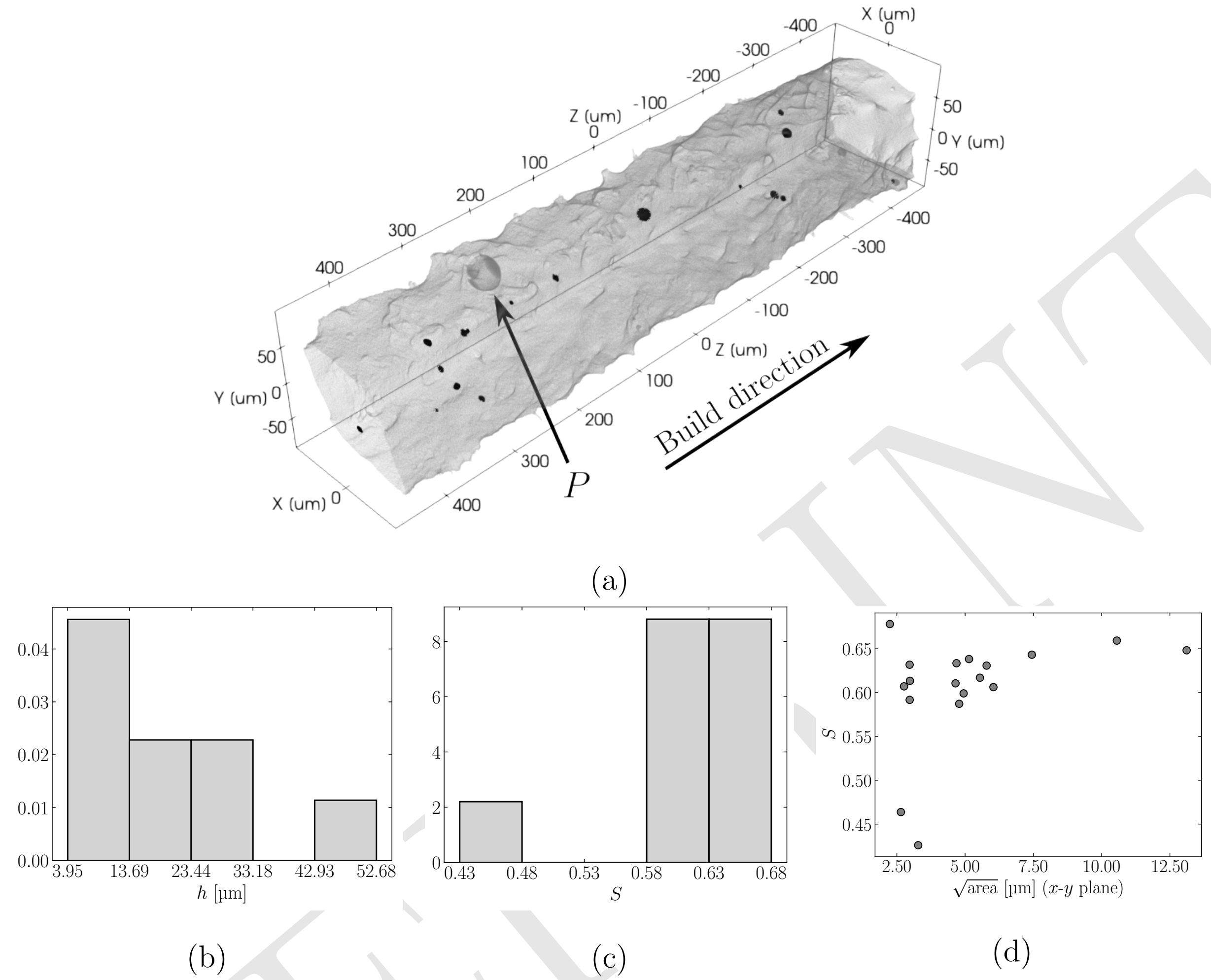

Figure 2: Results of the segmentation of CT images. (a) Segmented volume. The outer surface of the sample is rendered in transparent grey, whereas the detected pores are shown in black. The portion of the surface cavity labelled with P does not qualify as a pore, but it represents a surface cavity generated during the AM process. (b) Distribution of the minimum distance between the pores and outer surface, h. (c) Distribution of sphericity, S, computed as $S = \pi^{1/3}(6V)^{2/3}/A$, where V and A are the volume and external surface of each detected pore. (d) Distribution of S vs $\sqrt{\text{area}}$. This $\sqrt{\text{area}}$ is usually defined as the projection of A onto a plane of interest, e.g. the plane normal to the externally applied cyclic load. In this case, $\sqrt{\text{area}}$ is computed as the projection of A with respect to the $x - y$ plane, i.e. normal to the build direction.

representing spatial variations within intra-granular regions of similar orientation. Areas with distinct colour variations may indicate the formation of sub-grains cells, revealing heterogeneity at the inter-granular scale. Intuitively, regions with varying crystallographic orientations are linked with lattice distortions and can be linked to changes in lattice spacing,

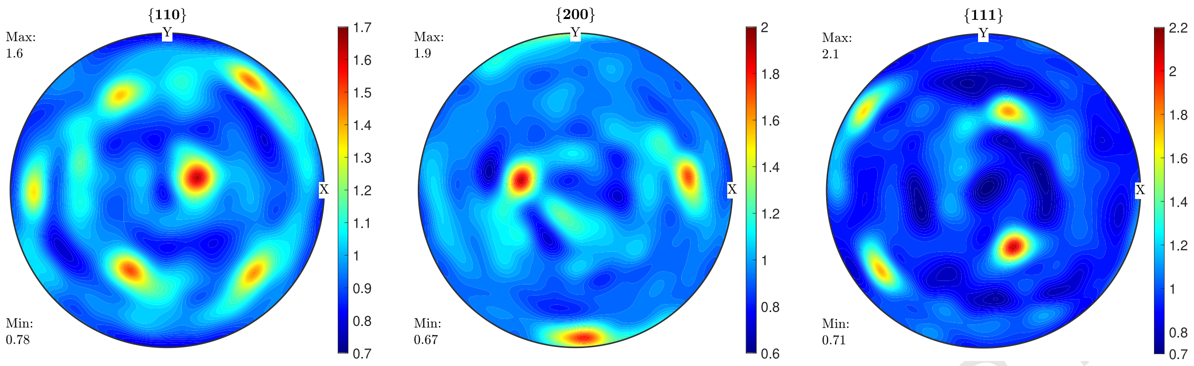

(a) (b) (c)

Figure 3: Pole figures of the ODF obtained from texture analysis. (a) {110}. (b) {200}. (c) {111}. Please note that the z-axis of the sample reference frame, which should nominally coincide with the sample build direction, was instead slightly misaligned, resulting in a small deviation between the reference frame and the actual build direction.

i.e. RS [8]. This phenomenon may result from both the accrual of local strains due to AM inhomogeneous thermal gradients, or differences in strain between grain interior and its boundary [57].

DFXM data was also post-processed to compute the misorientation ($\mathcal{N}$) according to [8, 38] (Fig. 5(a)), whereby the Geometrically Necessary Dislocations (GND) density, ρ_{GND}, was estimated (Fig. 5(b)). The misorientation turned out to be mostly confined in the range $[0°, 1°]$, which is corroborated by other studies in the literature [58, 59]. A closer inspection, shows the presence of areas with $\mathcal{N} \sim 0.6°$–seemingly low-angle grain boundaries–separating domains characterised by lower misorientation in qualitative agreement with [28]. Globally, this outcome suggests a uniform relative crystallographic orientation within the grain. Nonetheless, the retention of misorientation seems to indicate the continuation of local strain gradients, arising both from the fabrication process and from lattice incompatibilities amongst adjacent grains [60]. The organisation of ρ_{GND} is consistent with [28], although the previous investigation relied on EBSD measurements, hence ρ_{GND} solely referred to the surface of the sample. Similar to the misorientation distribution, ρ_{GND} arranges as regions of low density interspersed with areas exhibiting larger values of ρ_{GND}. Therefore, the 3D maps outline internal grain boundaries, where dislocations gathered, hinting at considerable

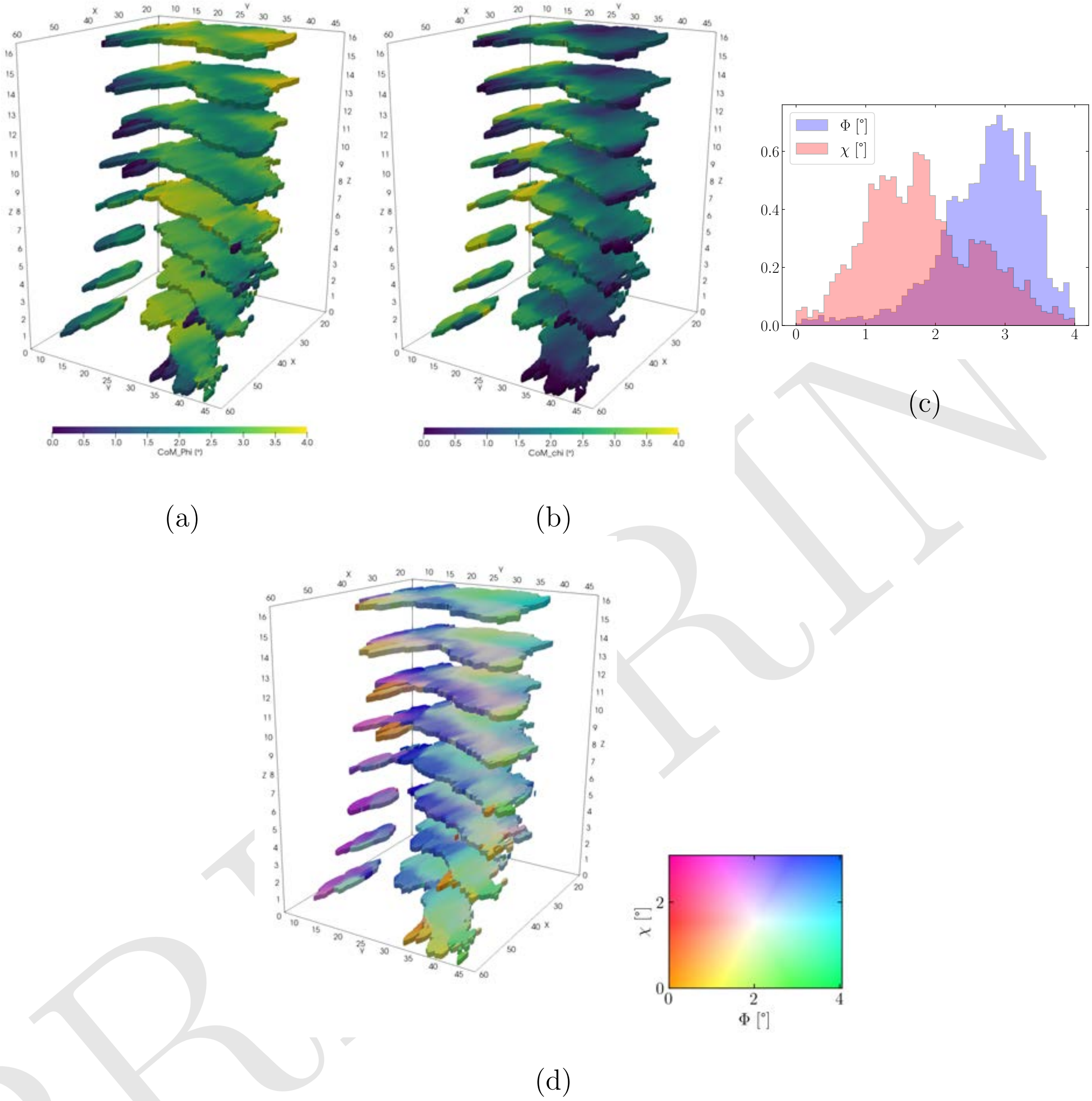

Figure 4: Results of the mosaicity scans. (a)-(b) Local crystal orientation quantified in terms of the centre-of-mass (CoM) at FWHM of the pixel-wise intensity distribution of the (200) reflection, recorded on the far-field detector as a function of the rocking angles Φ and χ, namely CoM_Φ and CoM_χ. (c) Histogram of CoM_χ and CoM_ϕ across all layers. (d) Mosaicity RGB map obtained by combining the previous CoMs data.

work-hardening and accumulated plastic strain, hence intra-granular RS [8]. Since the sample was in as-built condition, these features can primarily be attributed to the fabrication process itself. Furthermore, the characterisation of intra-granular dislocation density is of particular relevance, as ρ_{GND} is frequently adopted to describe the strengthening mechanisms in crystal plasticity models, both contributing to increasing the critical resolved shear stress and governing long-range internal stress (back stress) [61–64].

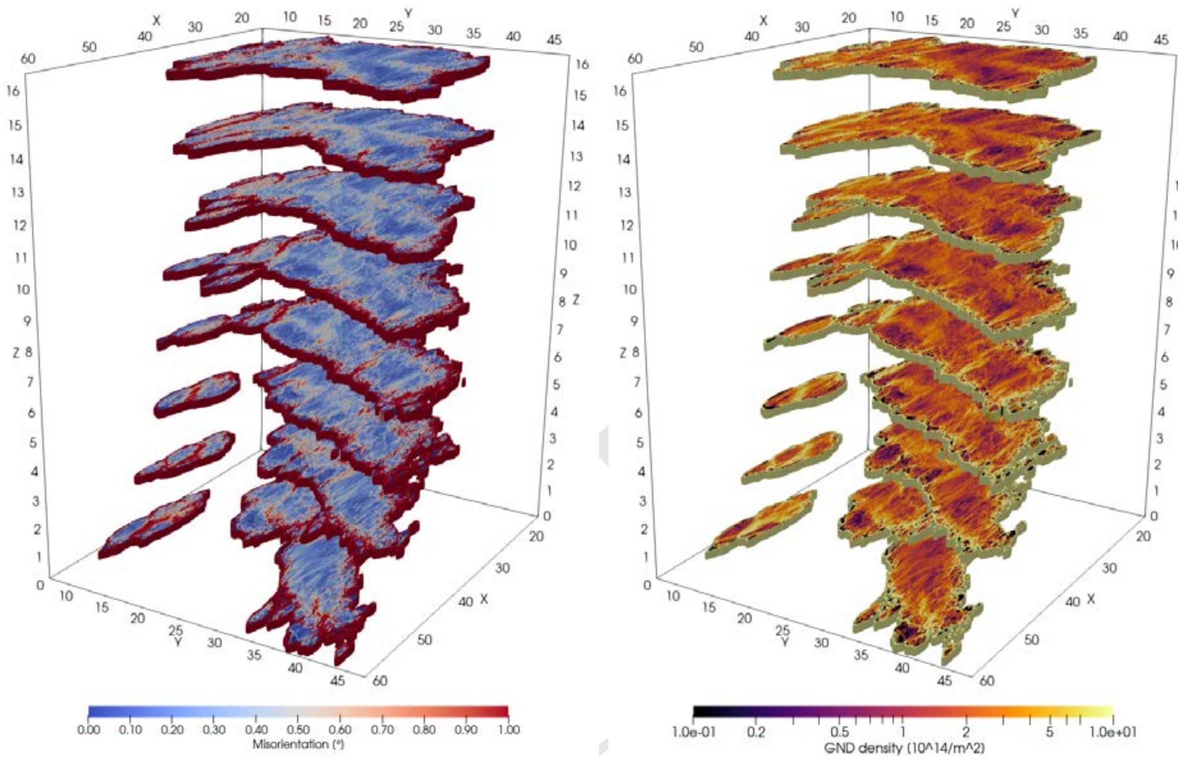

(a) (b)

Figure 5: (a) 3D map of misorientation distribution computed according to [8, 38], i.e. $\mathcal{N} = \sqrt{\Delta\Phi^2 + \Delta\chi^2}$, where $\Delta\Phi$ and $\Delta\chi$ are the differences in local orientation computed with respect to the pixel size. (b) 3D map of Geometrically Necessary Dislocation density (ρ_{GND}) distribution estimated through $\mathcal{N}$ by $\rho_{\mathrm{GND}} = \mathcal{N}/(10^{14} \cdot b\,t)$, where $b = 2.5 \cdot 10^{-10}$ m is the Burgers vector and $t = 100 \cdot 10^{-9}$ nm is the characteristic length scale over which the misorientation is measured, typically taken as the step size or thickness of the analysed region.

The experimental evidence indicates that RS is retained in the as-built material condition. As mentioned earlier, RS together with defects play a pivotal role in fatigue. Therefore, upon further targeted DFXM experiment a prospective development route would be the inference of RS descriptors, similarly to what proposed in [65]. When combined with prior information on pore and defect populations obtained from CT, these descriptors can be fed into predictive models to assess how the interplay between RS and defects governs fatigue behaviour, as well as how process parameters influence fatigue performance [66, 67].

In conclusion, the present work employed DFXM to investigate the orientation spread of a representative L-PBF AISI 316 grain in the bulk material. The analyses unveiled orientation spread across the grains up to 4°, together with mosaicity, whereby sub-granular structures with deviations in crystal lattice were identified. The processing of the data enabled the computation of misorientation and its correlation with dislocation density, showing elevated ρ_{GND} both within grains and along grain boundaries, in qualitative agreement with the authors' previous observations [28]. Besides proving the applicability of DFXM to this sort of material, the findings also provide, for the first time, insight into the intra-granular distribution of dislocation density in the bulk, which is not accessible with surface or destructive methods in a non-invasive manner. Texture analysis was conducted to characterise the orientation of the probed grain, showing $\{110\}$ as a preferred crystal orientational, which is substantiated by earlier findings [12, 28, 56]. Furthermore, additional CT investigation were carried out to segment the sample volume and statistically characterise its porosity. The pores are mainly located near the surface of the sample. Given their predominantly regular morphology, they were regarded as gas pores or key-hole defects. The output of this research represents valuable information for modelling the mechanical behaviour of the material, disclosing ρ_{GND} as a potential indicator of RS, which, in turn, warrants further quantitative assessment through dedicated DFXM axial strain scans.

CRediT authorship contribution statement

Alessandro Tognan. Conceptualisation, Methodology, Investigation, Validation, Data curation, Software, Writing – original draft, Writing – review & editing. **Can Yildirim.** Resources, Conceptualisation, Methodology, Investigation, Validation, Data curation, Software, Writing – original draft, Writing – review & editing. **Marco Pelegatti.** Investigation, Validation, Writing – review & editing. **Aditya Shukla.** Investigation, Data Curation, Writing – review & editing. **Emanuele Vaglio.** Resources, Investigation, Writing – review & editing. **Federico Scalzo.** Resources, Investigation, Writing – review & editing. **Enrico Salvati.** Resources, Conceptualisation, Methodology, Investigation, Validation, Writing – original draft, Writing – review & editing, Supervision, Funding acquisition.

Acknowledgements

This work has been supported by the following project "BREAKDOWN – Wide-ranging Probabilistic Physics-guided Machine Learning Approach to Break Down the Limits of Current Fatigue Predictive Tools for Metals – Project number: GA 101162848 – CUP: G23C24001880006" funded by the European Union. The authors acknowledge the provision of the beamtimes IH-MA-685 and IH-MA-749 at beamline ID03 of the European Synchrotron Radiation Facility. Can Yildirim and Aditya Shukla acknowledge support from the ERC Starting Grant nr. 10116911. The Laboratory for Advanced Mechatronics–LAMA FVG–of the University of Udine is gratefully acknowledged. LAMA FVG is an international research centre for product and process innovation where the three Universities of Friuli Venezia Giulia Region (Italy) synergistically cooperate for promoting R&D activities at academic and industrial levels.

Appendix A. 2D Layer-wise Maps of the Results

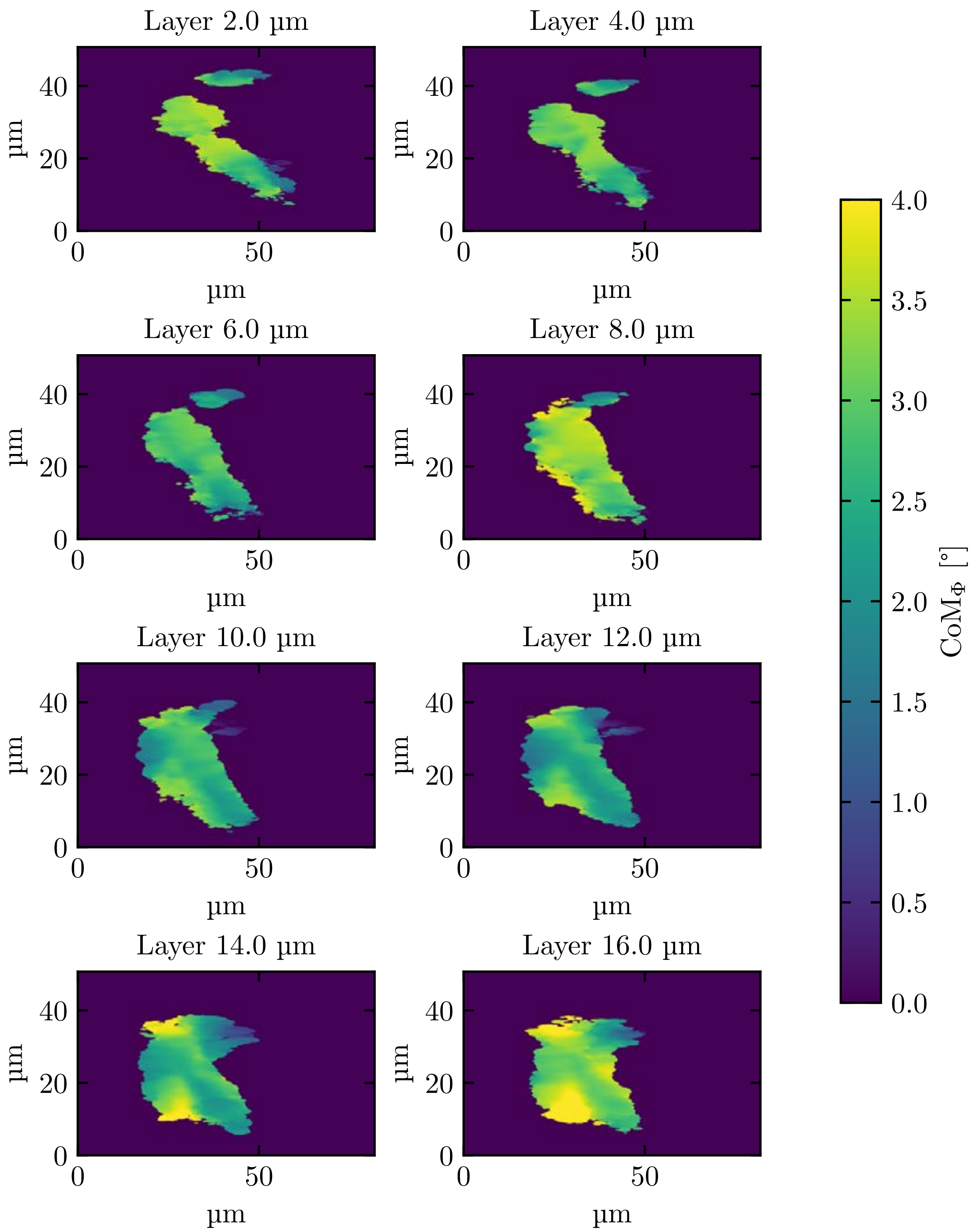

Figure A.6: Layer-wise orientation in terms of CoM_{ϕ}.

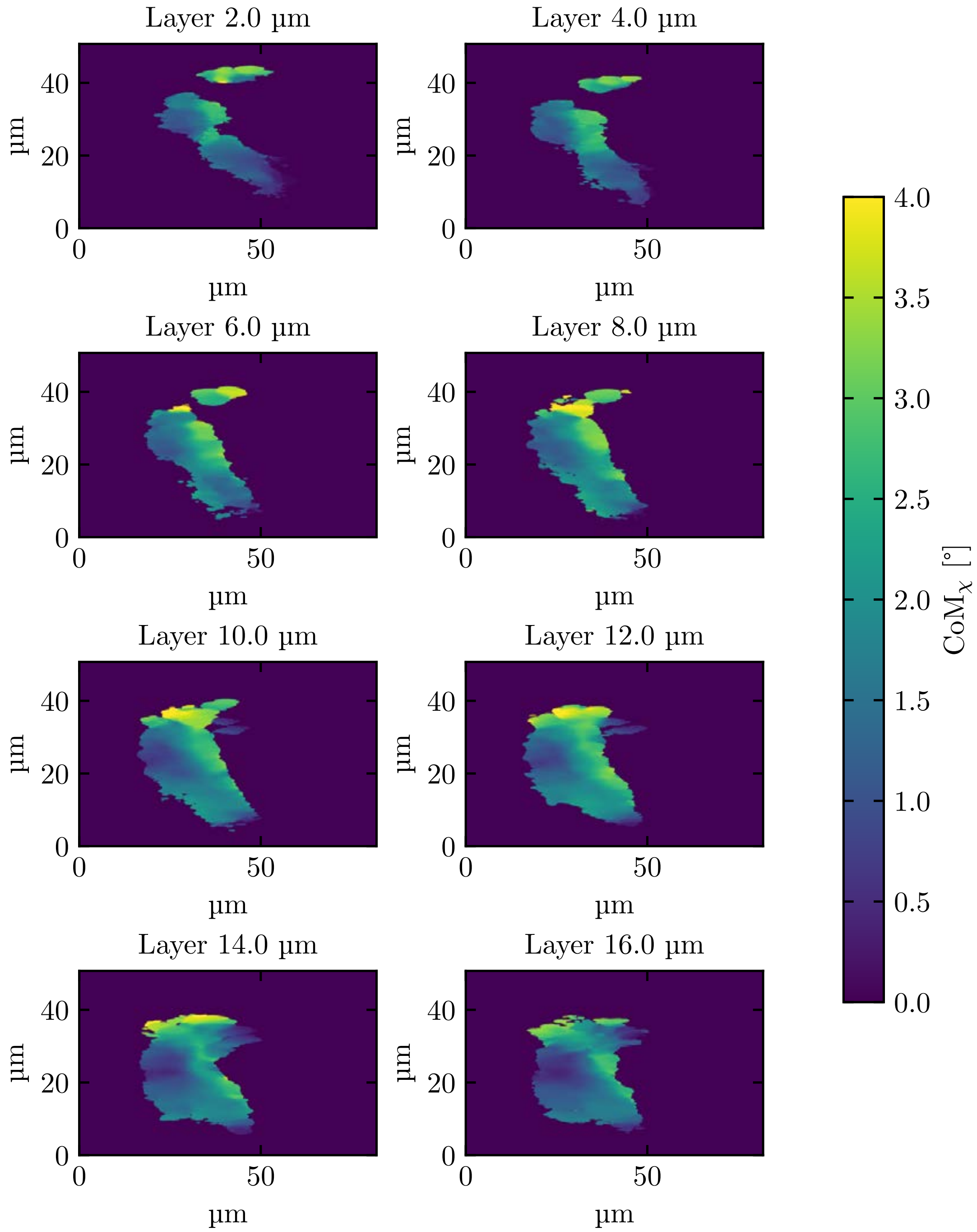

Figure A.7: Layer-wise orientation in terms of CoM_χ.

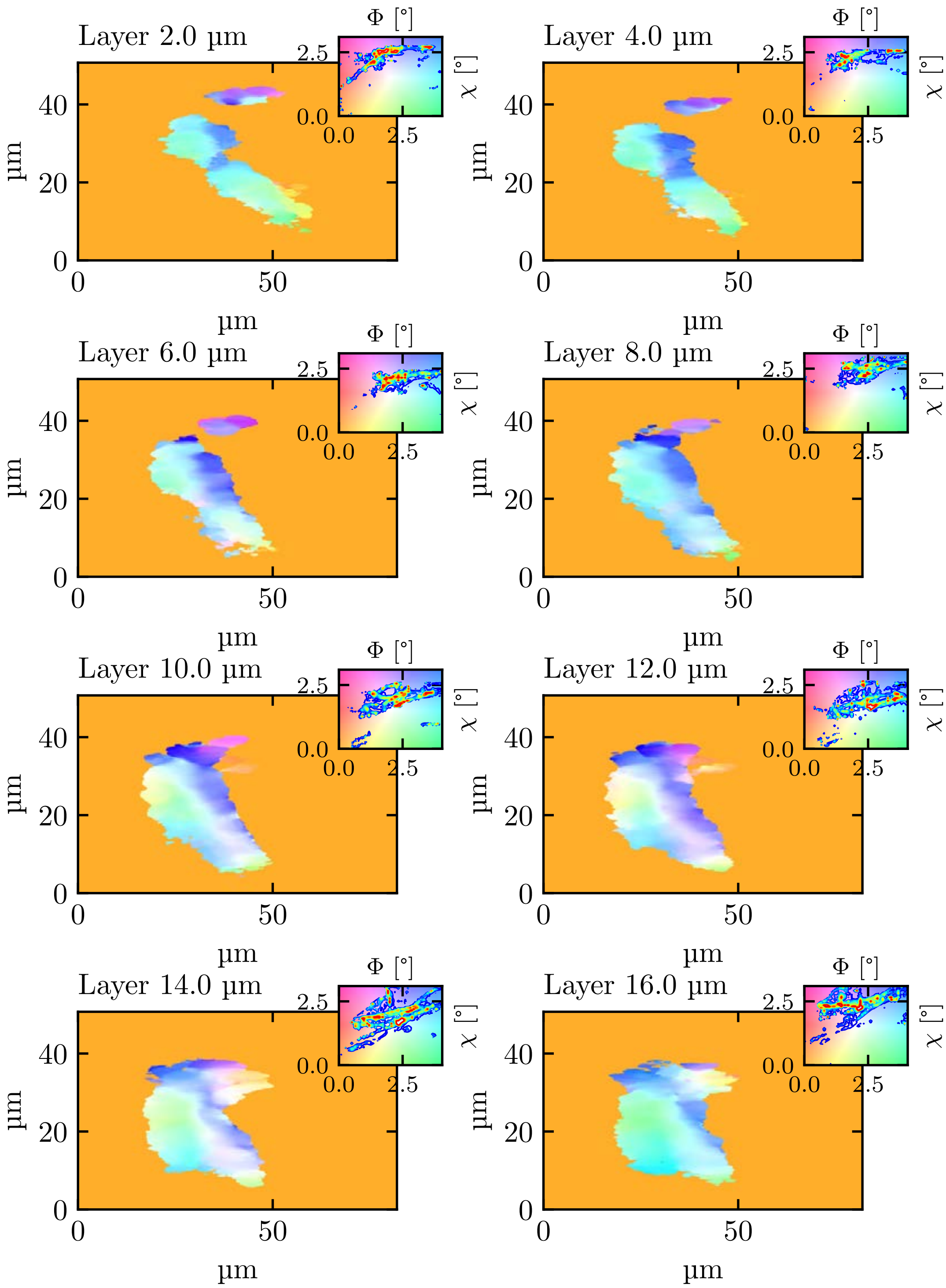

Figure A.8: Layer-wise mosaicity inferred from CoM_ϕ and CoM_χ

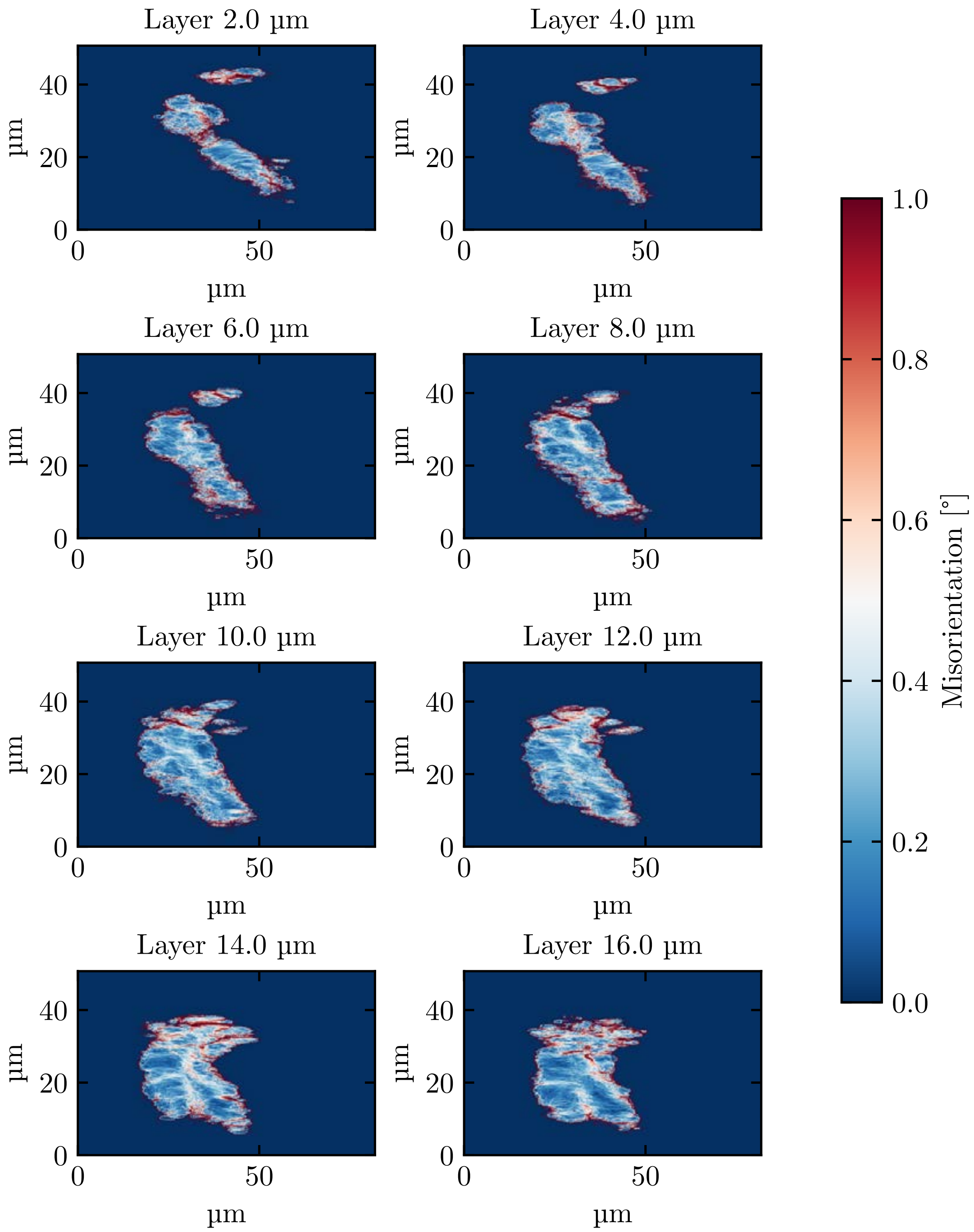

Figure A.9: Layer-wise misorientation.

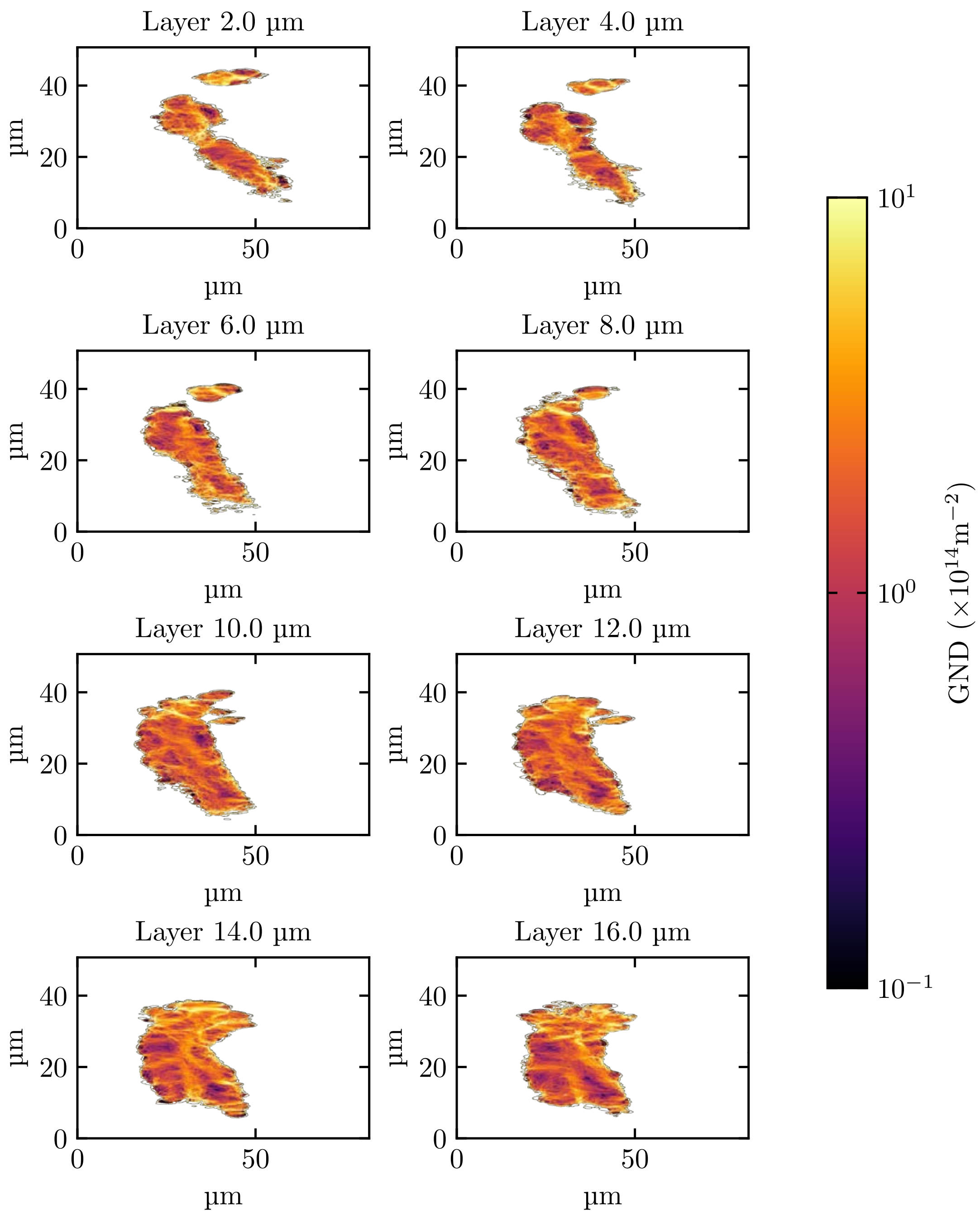

Figure A.10: Layer-wise misorientation Geometrically Necessary Dislocations density (ρ_{GND}).

References

[1] William E. Frazier. Metal Additive Manufacturing: A Review. *Journal of Materials Engineering and Performance*, 23(6):1917–1928, June 2014. doi: 10.1007/s11665-014-0958-z.

[2] Byron Blakey-Milner, Paul Gradl, Glen Snedden, Michael Brooks, Jean Pitot, Elena Lopez, Martin Leary, Filippo Berto, and Anton Du Plessis. Metal additive manufacturing in aerospace: A review. *Materials & Design*, 209:110008, November 2021. doi: 10.1016/j.matdes.2021.110008.

[3] P. Bajaj, A. Hariharan, A. Kini, P. Kürnsteiner, D. Raabe, and E.A. Jägle. Steels in additive manufacturing: A review of their microstructure and properties. *Materials Science and Engineering: A*, 772: 138633, January 2020. doi: 10.1016/j.msea.2019.138633.

[4] Danilo D'Andrea. Additive Manufacturing of AISI 316L Stainless Steel: A Review. *Metals*, 13(8):1370, July 2023. doi: 10.3390/met13081370.

[5] Anton du Plessis, Ina Yadroitsava, and Igor Yadroitsev. Effects of defects on mechanical properties in metal additive manufacturing: A review focusing on X-ray tomography insights. *Materials & Design*, 187:108385, February 2020. doi: 10.1016/j.matdes.2019.108385.

[6] Alessandro Tognan and Enrico Salvati. B-FADE: Bayesian-fatigue model estimator in Python and its application to the probabilistic estimation of El Haddad curves. *Scientific Reports*, 15(1):7106, February 2025. doi: 10.1038/s41598-024-82340-8.

[7] Emanuele Avoledo, Marco Petruzzi, Marco Pelegatti, Alessandro Tognan, Francesco De Bona, Michele Pressacco, Riccardo Toninato, and Enrico Salvati. Defect analysis by computed tomography in metallic materials: Optimisation, uncertainty quantification and classification. *Precision Engineering*, 97:235–248, 2026. doi: https://doi.org/10.1016/j.precisioneng.2025.09.008.

[8] Hongyu Chen, Dongdong Gu, Donghua Dai, Chenglong Ma, and Mujian Xia. Microstructure and composition homogeneity, tensile property, and underlying thermal physical mechanism of selective laser melting tool steel parts. *Materials Science and Engineering: A*, 682:279–289, January 2017. doi: 10.1016/j.msea.2016.11.047.

[9] Nima Haghdadi, Majid Laleh, Maxwell Moyle, and Sophie Primig. Additive manufacturing of steels: a review of achievements and challenges. *Journal of Materials Science*, 56(1):64–107, January 2021. doi: 10.1007/s10853-020-05109-0.

[10] Mustafa Güden, Hakan Yavaş, Ahmet Alptuğ Tanrıkulu, Alper Taşdemirci, Barış Akın, Samed Enser, Ayberk Karakuş, and Burcu Arslan Hamat. Orientation dependent tensile properties of a selective-laser-melt 316L stainless steel. *Materials Science and Engineering: A*, 824:141808, September 2021. doi: 10.1016/j.msea.2021.141808.

[11] Yulia O. Kuzminova, Stanislav A. Evlashin, and Andrey N. Belyakov. On the texture and strength of a 316L steel processed by powder bed fusion. *Materials Science and Engineering: A*, 913:147026,

October 2024. doi: 10.1016/j.msea.2024.147026.

[12] Jithin James Marattukalam, Dennis Karlsson, Victor Pacheco, Přemysl Beran, Urban Wiklund, Ulf Jansson, Björgvin Hjörvarsson, and Martin Sahlberg. The effect of laser scanning strategies on texture, mechanical properties, and site-specific grain orientation in selective laser melted 316L SS. *Materials & Design*, 193:108852, August 2020. doi: 10.1016/j.matdes.2020.108852.

[13] Olivier Andreau, Imade Koutiri, Patrice Peyre, Jean-Daniel Penot, Nicolas Saintier, Etienne Pessard, Thibaut De Terris, Corinne Dupuy, and Thierry Baudin. Texture control of 316L parts by modulation of the melt pool morphology in selective laser melting. *Journal of Materials Processing Technology*, 264:21–31, February 2019. doi: 10.1016/j.jmatprotec.2018.08.049.

[14] A. Leicht, C.H. Yu, V. Luzin, U. Klement, and E. Hryha. Effect of scan rotation on the microstructure development and mechanical properties of 316L parts produced by laser powder bed fusion. *Materials Characterization*, 163:110309, May 2020. doi: 10.1016/j.matchar.2020.110309.

[15] Xianglong Wang, Jose Alberto Muñiz-Lerma, Mohammad Attarian Shandiz, Oscar Sanchez-Mata, and Mathieu Brochu. Crystallographic-orientation-dependent tensile behaviours of stainless steel 316L fabricated by laser powder bed fusion. *Materials Science and Engineering: A*, 766:138395, October 2019. doi: 10.1016/j.msea.2019.138395.

[16] Deepak Kumar, Gyan Shankar, K.G. Prashanth, and Satyam Suwas. Control of texture and microstructure in additive manufacturing of stainless steel 316 L. *Journal of Alloys and Compounds*, 976:173040, March 2024. doi: 10.1016/j.jallcom.2023.173040.

[17] Leifeng Liu, Qingqing Ding, Yuan Zhong, Ji Zou, Jing Wu, Yu-Lung Chiu, Jixue Li, Ze Zhang, Qian Yu, and Zhijian Shen. Dislocation network in additive manufactured steel breaks strength–ductility trade-off. *Materials Today*, 21(4):354–361, May 2018. doi: 10.1016/j.mattod.2017.11.004.

[18] Dayong An, Yuhao Zhou, Xinxi Liu, Haoliang Wang, Shilei Li, Yao Xiao, Rui Li, Xifeng Li, Xianhong Han, and Jun Chen. Exploring structural origins responsible for the exceptional mechanical property of additively manufactured 316L stainless steel via in-situ and comparative investigations. *International Journal of Plasticity*, 170:103769, November 2023. doi: 10.1016/j.ijplas.2023.103769.

[19] Y.J. Yin, J.Q. Sun, J. Guo, X.F. Kan, and D.C. Yang. Mechanism of high yield strength and yield ratio of 316 L stainless steel by additive manufacturing. *Materials Science and Engineering: A*, 744: 773–777, January 2019. doi: 10.1016/j.msea.2018.12.092.

[20] Aliakbar Taghipour, Yousef Mazaheri, Jascha McDavid, Shahram Sheikhi, Moritz Braun, Junjun Shen, Benjamin Klusemann, and Sören Ehlers. Strengthening Mechanisms and Strain Hardening Behavior of 316L Stainless Steel Manufactured by Laser-Based Powder Bed Fusion. *Advanced Engineering Materials*, 25(4):2201230, February 2023. doi: 10.1002/adem.202201230.

[21] Ali Kazemi Movahed, Reza Ghanavati, Abdollah Saboori, and Luca Iuliano. A Review of Strategies for

In Situ Mitigating of Residual Stress in Laser-Based Metal Additive Manufacturing: Insights, Innovations, and Challenges. *Acta Metallurgica Sinica (English Letters)*, July 2025. doi: 10.1007/s40195-025-01902-5.

[22] Ali Tabatabaeian, Ahmad Reza Ghasemi, Mahmood M. Shokrieh, Bahareh Marzbanrad, Mohammad Baraheni, and Mohammad Fotouhi. Residual Stress in Engineering Materials: A Review. *Advanced Engineering Materials*, page 2100786, November 2021. doi: 10.1002/adem.202100786.

[23] Waseem Akhtar, Ismail Lazoglu, and Steven Y. Liang. Prediction and control of residual stress-based distortions in the machining of aerospace parts: A review. *Journal of Manufacturing Processes*, 76: 106–122, 2022. ISSN 1526-6125. doi: https://doi.org/10.1016/j.jmapro.2022.02.005.

[24] Alessandro Tognan, Noel Sheshi, Emanuele Vaglio, Vladimir Luzin, Daniel Hattingh, and Enrico Salvati. Multimodal experimental and numerical evaluation of Residual Stress in AA6082-T6 Friction Stir Welding pipe girths. *Journal of Materials Processing Technology*, 335:118665, January 2025. doi: 10.1016/j.jmatprotec.2024.118665.

[25] Majid Laleh, Esmaeil Sadeghi, Reynier I. Revilla, Qi Chao, Nima Haghdadi, Anthony E. Hughes, Wei Xu, Iris De Graeve, Ma Qian, Ian Gibson, and Mike Y. Tan. Heat treatment for metal additive manufacturing. *Progress in Materials Science*, 133:101051, March 2023. doi: 10.1016/j.pmatsci.2022.101051.

[26] Wei-Jen Lai, Avinesh Ojha, Ziang Li, Carlos Engler-Pinto, and Xuming Su. Effect of residual stress on fatigue strength of 316L stainless steel produced by laser powder bed fusion process. *Progress in Additive Manufacturing*, 6(3):375–383, August 2021. doi: 10.1007/s40964-021-00164-8.

[27] Wen Chen, Thomas Voisin, Yin Zhang, Jean-Baptiste Forien, Christopher M. Spadaccini, David L. McDowell, Ting Zhu, and Y. Morris Wang. Microscale residual stresses in additively manufactured stainless steel. *Nature Communications*, 10(1):4338, September 2019. doi: 10.1038/s41467-019-12265-8.

[28] Marco Beltrami, Marco Pelegatti, Michele Magnan, Alex Lanzutti, Maxim Avdeev, Vladimir Luzin, Matteo Leoni, Francesco De Bona, and Enrico Salvati. Microstructure and residual stress evolution during cyclic elastoplastic deformation of AISI316L fabricated via laser powder bed fusion. *Materials Science and Engineering: A*, 898:146416, April 2024. doi: 10.1016/j.msea.2024.146416.

[29] E. Salvati and A.M. Korsunsky. An analysis of macro- and micro-scale residual stresses of Type I, II and III using FIB-DIC micro-ring-core milling and crystal plasticity FE modelling. *International Journal of Plasticity*, 98:123–138, November 2017. doi: 10.1016/j.ijplas.2017.07.004.

[30] Y. Morris Wang, Thomas Voisin, Joseph T. McKeown, Jianchao Ye, Nicholas P. Calta, Zan Li, Zhi Zeng, Yin Zhang, Wen Chen, Tien Tran Roehling, Ryan T. Ott, Melissa K. Santala, Philip J. Depond, Manyalibo J. Matthews, Alex V. Hamza, and Ting Zhu. Additively manufactured hierarchical stainless steels with high strength and ductility. *Nature Materials*, 17(1):63–71, January 2018. doi:

10.1038/nmat5021.

[31] X. Wang, J.A. Muñiz-Lerma, O. Sanchez-Mata, M. Attarian Shandiz, N. Brodusch, R. Gauvin, and M. Brochu. Characterization of single crystalline austenitic stainless steel thin struts processed by laser powder bed fusion. *Scripta Materialia*, 163:51–56, April 2019. doi: 10.1016/j.scriptamat.2018.12.032.

[32] Y. Chen, Y.T. Tang, D.M. Collins, S.J. Clark, W. Ludwig, R. Rodriguez-Lamas, C. Detlefs, R.C. Reed, P.D. Lee, P.J. Withers, and C. Yildirim. High-resolution 3D strain and orientation mapping within a grain of a directed energy deposition laser additively manufactured superalloy. *Scripta Materialia*, 234: 115579, September 2023. ISSN 13596462. doi: 10.1016/j.scriptamat.2023.115579.

[33] M Kutsal, P Bernard, G Berruyer, P K Cook, R Hino, A C Jakobsen, W Ludwig, J Ormstrup, T Roth, H Simons, K Smets, J X Sierra, J Wade, P Wattecamps, C Yildirim, H F Poulsen, and C Detlefs. The ESRF dark-field x-ray microscope at ID06. *IOP Conference Series: Materials Science and Engineering*, 580(1):012007, August 2019. doi: 10.1088/1757-899X/580/1/012007.

[34] H. Simons, A. King, W. Ludwig, C. Detlefs, W. Pantleon, S. Schmidt, F. Stöhr, I. Snigireva, A. Snigirev, and H. F. Poulsen. Dark-field X-ray microscopy for multiscale structural characterization. *Nature Communications*, 6(1):6098, January 2015. doi: 10.1038/ncomms7098.

[35] Sara J. Irvine, Kento Katagiri, Trygve M. Ræder, Ulrike Boesenberg, Darshan Chalise, Jade I. Stanton, Dayeeta Pal, Jörg Hallmann, Gabriele Ansaldi, Felix Brauße, Jon H. Eggert, Lichao Fang, Eric Folsom, Morten Haubro, Theodor S. Holstad, Anders Madsen, Johannes Möller, Martin M. Nielsen, Henning F. Poulsen, Jan-Etienne Pudell, Angel Rodriguez-Fernandez, Frank Schoofs, Frank Seiboth, Yifan Wang, Wonhyuk Jo, Mohamed Youssef, Alexey Zozulya, Kristoffer Haldrup, and Leora E. Dresselhaus-Marais. Dark-field x-ray microscopy for 2D and 3D imaging of microstructural dynamics at the European x-ray free-electron laser. *Journal of Applied Physics*, 137(5):053106, February 2025. doi: 10.1063/5.0239034.

[36] Sven E. Gustafson, Wolfgang Ludwig, Raquel Rodriguez-Lamas, Can Yildirim, Katherine S. Shanks, Carsten Detlefs, and Michael D. Sangid. Revealing 3D intragranular micromechanical fields at triple junctions. *Acta Materialia*, 260:119300, November 2023. doi: 10.1016/j.actamat.2023.119300.

[37] Can Yildirim, Henning F. Poulsen, Grethe Winther, Carsten Detlefs, Pin H. Huang, and Leora E. Dresselhaus-Marais. Extensive 3D mapping of dislocation structures in bulk aluminum. *Scientific Reports*, 13(1):3834, March 2023. doi: 10.1038/s41598-023-30767-w.

[38] C. Yildirim, N. Mavrikakis, P.K. Cook, R. Rodriguez-Lamas, M. Kutsal, H.F. Poulsen, and C. Detlefs. 4D microstructural evolution in a heavily deformed ferritic alloy: A new perspective in recrystallisation studies. *Scripta Materialia*, 214:114689, June 2022. doi: 10.1016/j.scriptamat.2022.114689.

[39] Albert Zelenika, Adam André William Cretton, Felix Frankus, Sina Borgi, Flemming B. Grumsen, Can Yildirim, Carsten Detlefs, Grethe Winther, and Henning Friis Poulsen. Observing formation and evolution of dislocation cells during plastic deformation. *Scientific Reports*, 15(1):8655, March 2025.

doi: 10.1038/s41598-025-88262-3.

[40] H. Isern, T. Brochard, T. Dufrane, P. Brumund, E. Papillon, D. Scortani, R. Hino, C. Yildirim, R. Rodriguez Lamas, Y. Li, M. Sarkis, and C. Detlefs. The ESRF dark-field x-ray microscope at ID03. *Journal of Physics: Conference Series*, 3010(1):012163, May 2025. ISSN 1742-6596. doi: 10.1088/1742-6596/3010/1/012163. URL `https://doi.org/10.1088/1742-6596/3010/1/012163`.

[41] Marco Pelegatti, Denis Benasciutti, Francesco De Bona, Alex Lanzutti, Michele Magnan, Jelena Srnec Novak, Enrico Salvati, Francesco Sordetti, Marco Sortino, Giovanni Totis, and Emanuele Vaglio. On the factors influencing the elastoplastic cyclic response and low cycle fatigue failure of AISI 316L steel produced by laser-powder bed fusion. *International Journal of Fatigue*, 165:107224, December 2022. doi: 10.1016/j.ijfatigue.2022.107224.

[42] H. Payno, P. Paleo, Christian Nemoz, Alessandro Mirone, Pierre-Jean Gouttenoire, Jerome Lesaint, Wout De Nolf, and Thomas Vincent. tomwer, May 2025.

[43] Jean Ollion, Julien Cochennec, François Loll, Christophe Escudé, and Thomas Boudier. TANGO: a generic tool for high-throughput 3D image analysis for studying nuclear organization. *Bioinformatics*, 29(14):1840–1841, July 2013. ISSN 1367-4811, 1367-4803. doi: 10.1093/bioinformatics/btt276.

[44] C. Detlefs, A. Henningsson, B. Kanesalingam, A. a. W. Cretton, C. Corley-Wiciak, F. T. Frankus, D. Pal, S. Irvine, S. Borgi, H. F. Poulsen, C. Yildirim, and L. E. Dresselhaus-Marais. Oblique diffraction geometry for the observation of several non-coplanar Bragg reflections under identical illumination. *Journal of Applied Crystallography*, 58(4):1439–1446, August 2025. ISSN 1600-5767. doi: 10.1107/S1600576725005862.

[45] G. Ashiotis, A. Deschildre, Z. Nawaz, J. P. Wright, D. Karkoulis, F. E. Picca, and J. Kieffer. The fast azimuthal integration Python library: pyFAI. *Journal of Applied Crystallography*, 48(2):510–519, April 2015. ISSN 1600-5767. doi: 10.1107/S1600576715004306.

[46] F. Bachmann, Ralf Hielscher, and Helmut Schaeben. Texture analysis with mtex – free and open source software toolbox. In *Texture and Anisotropy of Polycrystals III*, volume 160 of *Solid State Phenomena*, pages 63–68. Trans Tech Publications Ltd, 3 2010. doi: 10.4028/www.scientific.net/SSP.160.63.

[47] J. Garriga Ferrer, R. Rodríguez-Lamas, H. Payno, W. De Nolf, P. Cook, V. A. Solé Jover, C. Yildirim, and C. Detlefs. darfix – data analysis for dark-field X-ray microscopy. *Journal of Synchrotron Radiation*, 30(3):527–537, May 2023. ISSN 1600-5775. doi: 10.1107/S1600577523001674.

[48] Bane Sullivan and Alexander Kaszynski. PyVista: 3D plotting and mesh analysis through a streamlined interface for the Visualization Toolkit (VTK). *Journal of Open Source Software*, 4(37):1450, May 2019. doi: 10.21105/joss.01450. URL `https://doi.org/10.21105/joss.01450`.

[49] James Ahrens, Berk Geveci, and Charles Law. ParaView: An End-User Tool for Large-Data Visualization. In *Visualization Handbook*, pages 717–731. Elsevier, 2005. doi: 10.1016/B978-012387582-2/50038-

1.

[50] Y. Murakami and M. Endo. Effects of defects, inclusions and inhomogeneities on fatigue strength. *International Journal of Fatigue*, 16(3):163–182, April 1994. ISSN 0142-1123. doi: 10.1016/0142-1123(94)90001-9.

[51] Uwe Zerbst, Giovanni Bruno, Jean-Yves Buffière, Thomas Wegener, Thomas Niendorf, Tao Wu, Xiang Zhang, Nikolai Kashaev, Giovanni Meneghetti, Nik Hrabe, Mauro Madia, Tiago Werner, Kai Hilgenberg, Martina Koukolíková, Radek Procházka, Jan Džugan, Benjamin Möller, Stefano Beretta, Alexander Evans, Rainer Wagener, and Kai Schnabel. Damage tolerant design of additively manufactured metallic components subjected to cyclic loading: State of the art and challenges. *Progress in Materials Science*, 121:100786, August 2021. ISSN 0079-6425. doi: 10.1016/j.pmatsci.2021.100786.

[52] Niloofar Sanaei and Ali Fatemi. Defects in additive manufactured metals and their effect on fatigue performance: A state-of-the-art review. *Progress in Materials Science*, 117:100724, April 2021. ISSN 00796425. doi: 10.1016/j.pmatsci.2020.100724.

[53] S. Romano, A. Brückner-Foit, A. Brandão, J. Gumpinger, T. Ghidini, and S. Beretta. Fatigue properties of AlSi10Mg obtained by additive manufacturing: Defect-based modelling and prediction of fatigue strength. *Engineering Fracture Mechanics*, 187:165–189, January 2018. ISSN 00137944. doi: 10.1016/j.engfracmech.2017.11.002.

[54] S. Romano, A. Abel, J. Gumpinger, A.D. Brandão, and S. Beretta. Quality control of AlSi10Mg produced by SLM: Metallography versus CT scans for critical defect size assessment. *Additive Manufacturing*, 28:394–405, August 2019. ISSN 22148604. doi: 10.1016/j.addma.2019.05.017.

[55] Yukitaka Murakami. Material defects as the basis of fatigue design. *International Journal of Fatigue*, 41:2–10, August 2012. ISSN 01421123. doi: 10.1016/j.ijfatigue.2011.12.001. URL `https://linkinghub.elsevier.com/retrieve/pii/S0142112311003161`.

[56] Marco Pelegatti, Jaromír Brůža, Michal Jambor, Filip Šiška, and Jiří Man. On microstructure evolution and damage onset in 316l steel produced by laser-powder bed fusion during the early stages of low cycle fatigue loading. *Materials Characterization*, 228:115448, October 2025. ISSN 1044-5803. doi: 10.1016/j.matchar.2025.115448.

[57] K. Hlushko, J. Keckes, G. Ressel, J. Pörnbacher, W. Ecker, M. Kutsal, P.K. Cook, C. Detlefs, and C. Yildirim. Dark-field X-ray microscopy reveals mosaicity and strain gradients across sub-surface TiC and TiN particles in steel matrix composites. *Scripta Materialia*, 187:402–406, October 2020. doi: 10.1016/j.scriptamat.2020.06.053.

[58] Thomas Voisin, Jean-Baptiste Forien, Aurelien Perron, Sylvie Aubry, Nicolas Bertin, Amit Samanta, Alexander Baker, and Y. Morris Wang. New insights on cellular structures strengthening mechanisms and thermal stability of an austenitic stainless steel fabricated by laser powder-bed-fusion. *Acta Mate-*

rialia, 203:116476, January 2021. doi: 10.1016/j.actamat.2020.11.018.

[59] Siqi Chen, Guoqiang Ma, Guilin Wu, Andrew Godfrey, Tianlin Huang, and Xiaoxu Huang. Strengthening mechanisms in selective laser melted 316L stainless steel. *Materials Science and Engineering: A*, 832:142434, January 2022. doi: 10.1016/j.msea.2021.142434.

[60] Can Yildirim, Aditya Shukla, Yubin Zhang, Nikolas Mavrikakis, Louis Lesage, Virginia Sanna, Marilyn Sarkis, Yaozhu Li, Michela La Bella, Carsten Detlefs, and Henning Friis Poulsen. 3D/4D imaging of complex and deformed microstructures with pink-beam dark field X-ray microscopy. *Communications Materials*, 6(1):198, August 2025. doi: 10.1038/s43246-025-00926-9.

[61] Michael Salvini, Nicolò Grilli, Eralp Demir, Siqi He, Tomas Martin, Peter Flewitt, Mahmoud Mostafavi, Christopher Truman, and David Knowles. Effect of grain boundary misorientation and carbide precipitation on damage initiation: A coupled crystal plasticity and phase field damage study. *International Journal of Plasticity*, 172:103854, January 2024. doi: 10.1016/j.ijplas.2023.103854.

[62] Ritwik Bandyopadhyay, Sven E. Gustafson, Kartik Kapoor, Diwakar Naragani, Darren C. Pagan, and Michael D. Sangid. Comparative assessment of backstress models using high-energy X-ray diffraction microscopy experiments and crystal plasticity finite element simulations. *International Journal of Plasticity*, 136:102887, January 2021. doi: 10.1016/j.ijplas.2020.102887.

[63] Anxin Ma and Alexander Hartmaier. On the influence of isotropic and kinematic hardening caused by strain gradients on the deformation behaviour of polycrystals. *Philosophical Magazine*, 94(2):125–140, 2014. doi: 10.1080/14786435.2013.847290.

[64] F. P. E. Dunne, R. Kiwanuka, and A. J. Wilkinson. Crystal plasticity analysis of micro-deformation, lattice rotation and geometrically necessary dislocation density. *Proceedings of the Royal Society A: Mathematical, Physical and Engineering Sciences*, 468(2145):2509–2531, September 2012. doi: 10.1098/rspa.2012.0050.

[65] Yaozhong Zhang, James Ball, Axel Henningsson, Jon Wright, Lucero Lopez, Dillon Jobes, Henry Proudhon, and Jerard V. Gordon. Unveiling 3D sub-grain residual stresses in as-built additively manufactured steel using scanning 3DXRD. *Materials Research Letters*, 13(7):700–708, July 2025. ISSN 2166-3831. doi: 10.1080/21663831.2025.2502502.

[66] A Ciampaglia, A. Tridello, D. S. Paolino, and F. Berto. Data driven method for predicting the effect of process parameters on the fatigue response of additive manufactured AlSi10Mg parts. *International Journal of Fatigue*, 170:107500, May 2023. ISSN 0142-1123. doi: 10.1016/j.ijfatigue.2023.107500.

[67] Lanyi Wang, Shun-Peng Zhu, Changqi Luo, Ding Liao, and Qingyuan Wang. Physics-guided machine learning frameworks for fatigue life prediction of AM materials. *International Journal of Fatigue*, page 107658, March 2023. ISSN 01421123. doi: 10.1016/j.ijfatigue.2023.107658.